

WIND TUNNEL MODEL STUDY OF TURBULENCE REGIME IN THE ATMOSPHERIC CONVECTIVE BOUNDARY LAYER

E. FEDOROVICH AND R. KAISER
*Institute of Hydrology and Water Resources Planning
Karlsruhe University
Kaiserstrasse 12, 76128 Karlsruhe, Germany*

Abstract

Results from a wind tunnel model of the sheared atmospheric convective boundary layer (CBL) are presented and discussed. The model is realized in the thermally stratified wind tunnel of the Institute of Hydrology and Water Resources Planning (IHW), University of Karlsruhe. Design of the wind tunnel, and the technique employed for velocity and temperature measurements are described. The performed experiments reproduce convective conditions in the atmosphere when both capping inversion and hydrostatic stability of the free-atmosphere air are not very strong. Under such conditions, the turbulence regime in the CBL is mainly determined by the bottom-up convective and shear forcings, whereas the heat flux of entrainment and temperature fluctuation magnitude within the inversion layer are comparatively small. Temporal averaging has been employed for deriving turbulence statistics from the velocity and temperature time series measured. These statistics are compared with their counterparts from atmospheric measurements, and from numerical and laboratory model studies.

Surface shear and elevated shear were found to be essential factors modifying the CBL turbulence regime. The elevated shear turned out to be an inhibitor of entrainment at the CBL top. Turbulence enhancement has been observed in the transition zone between the unmixed convective layer in the neutral environment and the well-mixed CBL capped by a temperature inversion.

The turbulence spectra obtained display short but pronounced inertial intervals in large-wavenumber ranges. The characteristic value of the turbulent Reynolds number Re_t in the simulated CBL is $3 \cdot 10^3$. The vertical to horizontal velocity spectral ratio is slightly higher than the local-isotropy value of $4/3$. Velocity spectra measured in the lower portion of the CBL show the buoyancy to be the dominant factor of turbulence production at smaller wavenumbers, while the shear contribution increases with the wavenumber growth. The combined effect of buoyant and shear forcings apparently leads to elongation and flatness of the production ranges in the velocity spectra. The inertial-subrange theory relationships have been used for evaluation of the turbulence dissipation rates from the velocity spectra. The turbulence kinetic energy dissipation rates in the CBL with shear were found to be comparatively large over the whole turbulent region.

1. Introduction

The principal feature of the atmospheric convective boundary layer (CBL) is the strong turbulent mixing occupying the main portion of the layer in the vertical. This mixing is chiefly maintained by buoyant plumes and thermals (warm updrafts), rising from the warm underlying surface, and associated descending motions (cool downdrafts). Wind shear is a secondary mechanism of turbulence generation in the atmospheric CBL.

The CBL mixed core, where horizontally (or temporally) averaged meteorological variables like potential temperature, specific humidity, and wind velocity are nearly height-constant, is commonly called the mixed layer. This layer is separated from the underlying surface by a relatively shallow surface layer, within which meteorological variables change sharply from their near-surface values to the mixed-layer ones. The interfacial (inversion) layer, also called the entrainment layer (zone), is located above the mixed layer. In the entrainment layer, the energy of thermals is expended for their penetration into the stably stratified atmospheric air aloft and for mixing (entraining) it downwards.

Entrainment is accompanied by the downward transport of heat from the warmer outer flow region into the mixed layer. Thus, the entrainment zone corresponds to the range of heights with negative kinematic heat flux. Entrainment of more buoyant air into the mixed layer leads to the increase of the CBL depth.

Typically, the interfacial (entrainment) layer is characterized by strong vertical gradients of averaged meteorological quantities. Wind shear across the interfacial layer (the so-called elevated shear) contributes to the turbulence production in the upper part of the CBL and, presumably, can modify the regime of entrainment. The entrainment-layer depth is quite variable, but usually smaller than the mixed-layer depth. Towards the top of the interfacial layer, turbulence decays and turbulent transport becomes negligible.

Observations of the atmospheric CBL are presented in this volume by D. Lenschow [26].

When the buoyant (convective) production of turbulence in the CBL dominates the mechanical (shear) production, the CBL can be considered as shear-free. This CBL case has been simulated in numerous laboratory water tank experiments pioneered by J. Deardorff and his colleagues (Deardorff *et al.* [10,11], Willis and Deardorff [56], Deardorff and Willis [9]; see also reports from the water tank studies of Kumar and Adrian [25] Adrian *et al.* [1], and Cenedese and Querzoli [6]). Meanwhile the sheared CBL, which is a much more common case in the atmosphere, was left beyond the scope of water tank experiments.

Systematic wind tunnel studies of the atmospheric convective turbulence have been carried out by only a few research teams over the world (Rey *et al.* [45], Ogawa *et al.* [36], and Poreh and Cermak [41]). The analysis of the operating ranges of the existing wind tunnel facilities for simulating the atmospheric CBL, (Meroney and Melbourne [32], see also the paper by Meroney [31] in this volume), gives an idea of the multitude of technical problems awaiting investigators attempting to reproduce details of the CBL turbulence in wind tunnels. Inspection of available data from wind tunnel experiments makes evident that in most of them the flow structure was not appropriately resolved for making quantitative conclusions concerning the CBL turbulence regime. Among the other problems of wind tunnel CBL modeling are size limitations (usually, a very long tunnel is needed to generate a sufficiently deep CBL), and difficulties with matching the model to prototype scale requirements for a number of important

integral parameters of the CBL, namely, for the inversion strength, the boundary-layer depth, the temperature gradient in the turbulence-free layer, and the surface heat flux.

Analysis of the above problems, and the experience accumulated from water tank and wind tunnel model studies of atmospheric convection at the Institute of Hydrology and Water Resources Planning (IHW), Karlsruhe University, (see paper by E. Plate [40] in this volume), enabled the development of a concept of the thermally stratified wind tunnel with preshaped vertical temperature and velocity profiles at the inlet of the test section. The preshaped profiles roughly correspond to vertical distributions of temperature and velocity in the developed atmospheric CBL. Adjustment of the preshaped boundary layer to the buoyant and shear forcings takes place while the flow proceeds downstream over the heated, aerodynamically rough floor of the test section. This method minimizes the fetch, over which a quasi-equilibrium and quasi-homogeneous turbulence regime in the simulated CBL is achieved. By varying the shapes of the temperature and velocity profiles at the test section inlet, different CBL flow regimes with combined buoyant and shear forcings can be investigated. This is a step forward compared with the pure shear-free CBL cases reproduced in the water tank models.

Study of the mean-flow characteristics and turbulence statistics in the IHW wind tunnel was reported by Fedorovich *et al.* [15]. This study was followed by investigation of spectral properties of the CBL turbulence by Kaiser and Fedorovich [23].

The simulation approach employed in the IHW tunnel allows generation of a quasi-stationary CBL, which develops longitudinally and grows by the advection-type entrainment of warmer air from upper turbulence-free layers into the convectively mixed layer. A CBL of similar type develops in the atmosphere when a neutrally stratified air mass is advected over a heated terrain. Preceding model studies of the CBL, both numerical and laboratory, dealt mostly with cases of nonstationary, horizontally quasi-homogeneous CBL. Under general conditions, in the presence of mean wind and over a nonuniform underlying surface, the atmospheric CBL grows by both advection and nonstationary mechanisms.

Due to the quasi-stationarity of the simulated CBL, the turbulence statistics in the wind tunnel model are calculated through temporal averaging. In studies of the nonstationary CBL the statistics are commonly obtained through area averaging.

The turbulence regime in the wind tunnel model of the sheared atmospheric CBL is analyzed and discussed in the present paper. Before showing the simulation results, we will give a brief description of the technique and methods employed for velocity and temperature measurements in the tunnel. The technique for the flow visualization will be considered as well, and some visualized flow patterns will be shown. Particular attention will be devoted to the comparison of the turbulence statistics and spectra obtained in the tunnel with their counterparts derived from atmospheric measurements, and from numerical and water tank models of the atmospheric CBL.

2. Experimental Setup and Measurement Technique

The thermally stratified wind tunnel of the IHW is specially designed for simulating turbulent flow and dispersion in the sheared atmospheric CBL capped by a temperature inversion. The

design features of the tunnel are considered in detail by Rau *et al.* [43], Poreh *et al.* [42], and Rau and Plate [44].

The tunnel is of the closed-circuit type, (see Fig. 1), which allows minimization of the energy supply necessary for maintaining a stable thermal regime in the flow. The test section of the tunnel is 10 m long, 1.5 m wide, and 1.5 m high. The return section is subdivided into 10 individually insulated layers. Each 15-cm deep layer is operated by its own fan and heating element. The system of fans and heating elements is driven by a feedback control system. In this way, the vertical velocity and temperature distributions at the inlet of the test section can be preset and kept constant. The test section floor, which is constructed of aluminum plates, is also heated in a controlled way to ensure a constant heat flux through the bottom. The floor roughness may be regulated by employing variable-size roughness elements mounted on the floor.

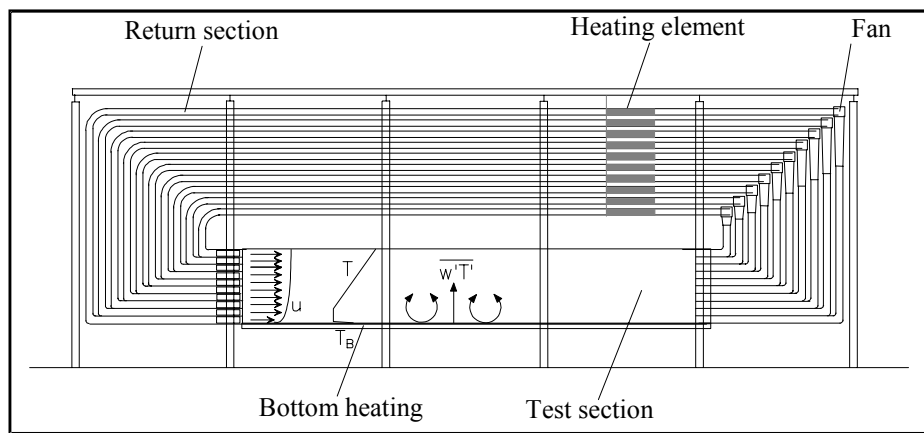


Figure 1. Schematic cut of the thermally stratified wind tunnel along the central longitudinal plane.

The design of the tunnel gives the opportunity of reproducing convective regimes with different extents of shear contribution to the turbulence production and generating a developed CBL over comparatively short fetches.

At the same time, there are certain limitations imposed on the flow parameters in the tunnel and, consequently, on the simulated turbulence regimes. In particular, the maximum inversion elevation that can be presently achieved in the tunnel is about 0.5 m, (remember that the height of the test section is 1.5 m). Maximum values of the temperature gradient in the outer flow above the inversion, and of the temperature increment across the inversion layer are 100 K/m and 100 K, respectively. The flow velocity at the inlet can be varied within the interval from 0.5 m/s to 2 m/s. The upper limit for the heat flux through the bottom is 1.5 K·m/s.

2.1. SCALING CONSIDERATIONS

To relate the simulated CBL to its atmospheric prototype, a set of nondimensional similarity parameters must be elaborated. Following Deardorff *et al.* [11], Zilitinkevich [60], and Fedorovich and Mironov [16] we will use for this purpose two Richardson numbers, $Ri_{\Delta T}$ and

Ri_N . The first of them is based on the temperature increment ΔT across the inversion layer: $Ri_{\Delta T} = \beta w_*^{-2} z_i \Delta T$. The second represents the effect of stable stratification (characterized by the value of buoyancy frequency N) above the interfacial layer: $Ri_N = N^2 z_i^2 w_*^{-2}$. The other two scaling parameters entering $Ri_{\Delta T}$ and Ri_N are the CBL depth z_i and the Deardorff [8] convective velocity scale $w_* = (\beta Q_s z_i)^{1/3}$, in which $\beta = g / T_0$ is the buoyancy parameter (g is the acceleration due to the gravity, T_0 is the reference temperature value), and Q_s is the near-surface value of the turbulent kinematic heat flux. The above Richardson numbers represent only the buoyant forcing in the CBL. To account for the effects of wind shear at the surface, these parameters must be complemented by the ratio u_* / w_* , which characterizes the proportion between dynamic (u_* is the friction velocity) and buoyant contributions to the turbulence production in the CBL (Meroney and Melbourne [32]).

Another important dimensionless parameter of the CBL turbulence regime is the Reynolds number, $Re = U_c L_c / \nu$, where U_c and L_c are characteristic velocity and length scales of the flow, respectively, and ν is the kinematic viscosity of the air.

In the atmospheric CBL, typical $Ri_{\Delta T}$ and Ri_N values are within the range of 0 to 100, and Re is of the order 10^8 . In the IHW wind tunnel, a maximum $Ri_{\Delta T}$ of about 10, and a maximum Ri_N of about 20 can presently be achieved. This corresponds to atmospheric convection cases with comparatively weak damping effects of stable stratification in the upper portion of the CBL and above the convection zone. In the wind tunnel CBL, Re varies within the range of 10^3 to 10^5 , depending on the length and velocity scales chosen. With such Re values, the reproduced turbulent regime can be roughly considered Re independent.

Turbulence production in the CBL is buoyancy-dominated when the ratio u_* / w_* is sufficiently small. Based on classification proposed by Holtslag and Nieuwstadt [19], $u_* / w_* = 0.34$ may be obtained as a conventional boundary value separating the regimes of sheared and shear-free convection. Typical values of u_* / w_* in the wind tunnel are within the range of 0.2 to 0.5, that is near and above the boundary value for shear effects.

Temporal and spatial scales of turbulent motions in the simulated CBL may be related using the Taylor translation hypothesis (Willis and Deardorff [57]). It was shown in Fedorovich *et al.* [15] that this hypothesis is satisfied fairly well in the wind tunnel CBL where velocity turbulent fluctuations are typically small compared to the mean-flow velocity.

2.2. MEASUREMENT AND VISUALIZATION TECHNIQUE

2.2.1. Laser Doppler Velocimetry

The laser Doppler velocimetry (LDV) provides a method for measuring flow velocity with high accuracy and spatial resolution. The LDV measuring signal is independent on temperature fluctuations which is of particular importance in high-temperature wind tunnel flow. All constants of the LDV system are usually known and thus time-consuming calibrations, characteristic of the hot-wire anemometry, can be avoided in the LDV measurement

procedures. Comprehensive explanations of the LDV principles are given in literature, see *e.g.* Drain [13], Wiedemann [55], Durst *et al.* [14], and Ruck [46].

The two-beam configuration is the most common LDV setup. Its schematic is shown in Fig. 2. All velocity measurements in the wind tunnel CBL were performed with this setup.

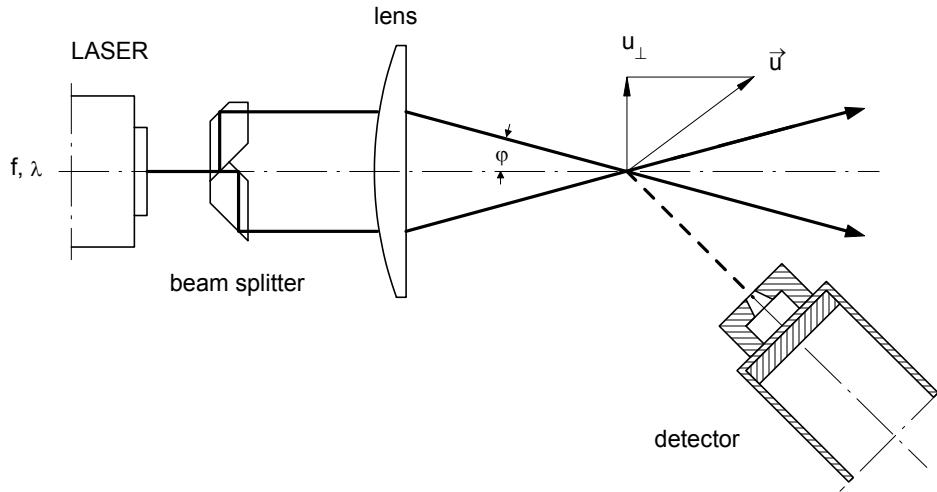


Figure 2. A dual-beam laser Doppler velocimeter, after Ruck [46].

The flow velocity is determined by the LDV from the speed of small particles transported by the flow. Such particles are produced using a 5% aqueous solution of Na_2SO_4 . This solution is injected into the flow at the test section inlet by means of jet atomizers. In the test section, the water component of the spray droplets evaporates and the flow is seeded by small salt crystals. The Na_2SO_4 crystals have a refraction index of 1.5, and thus scatter light well. The Na_2SO_4 compound is neither toxic nor corrosive. Besides that, it is not hygroscopic, and comparatively cheap.

The frequency response of the velocity amplitudes of the particle and of the flow can be roughly estimated as (Domnik [12])

$$\frac{\hat{u}_P}{\hat{u}_F} = \frac{1}{\sqrt{1 + (\omega\tau)^2}}. \quad (1)$$

Here, the indices P and F refer to the particle and to the flow, respectively, \hat{u}_P / \hat{u}_F is the frequency response of the velocity amplitudes, ω is the circular frequency, $\tau = (2/9)(r^2 / \nu)(\rho_P / \rho_F)$ is the time constant of the particle (relaxation time), r is the radius of the particle, and ρ_P , ρ_F are the densities of the particle material and of the transporting fluid, respectively.

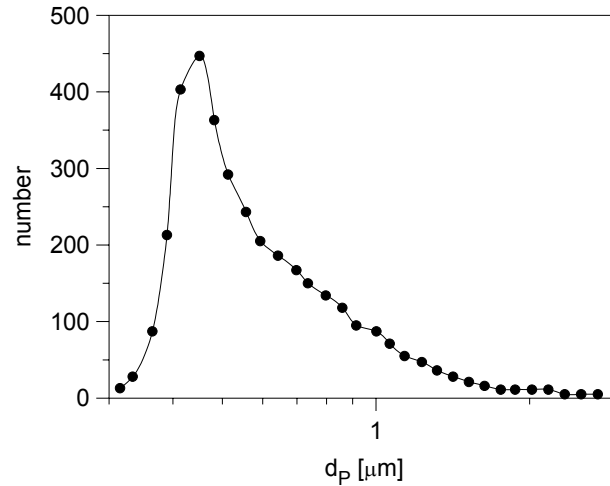


Figure 3. Size distribution of the seeding particles.

Figure 3 shows the size (diameter) distribution of the Na_2SO_4 seeding particles. Most of the particles have a diameter between $0.3 \mu\text{m}$ and $1.5 \mu\text{m}$ which gives a relaxation time within the range of $1 \mu\text{s}$ to $20 \mu\text{s}$. The particle sinking velocity in a calm fluid, $u_E = (1 - \rho_F / \rho_P)g\tau$, is therefore between $10 \mu\text{m/s}$ and $200 \mu\text{m/s}$. For the cut-off frequency $f_c = 1 / (2\pi\tau)$ we obtain an estimate between 8 KHz and 160 KHz.

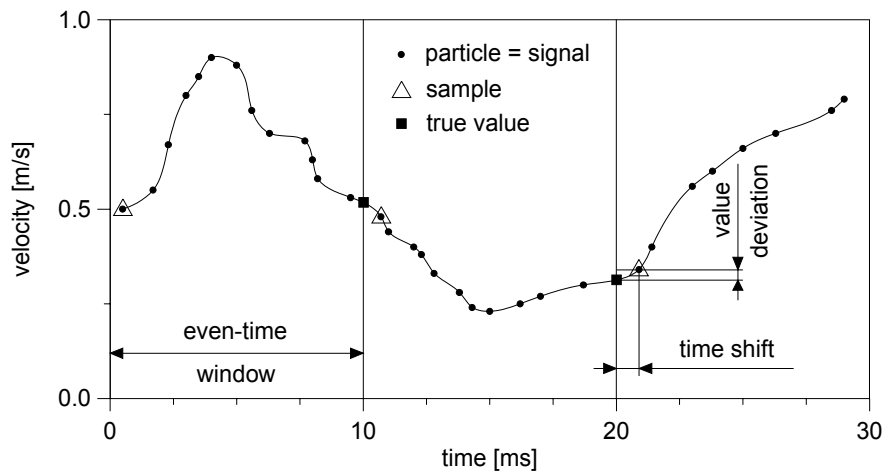


Figure 4. Quasi-equidistant sampling with LDV.

To perform quasi-equidistant velocity field sampling, the LDV processor was operated in the even-time mode, see Fig. 4. In each even-time window corresponding to the sampling time interval the average amount of arriving particles (and therefore the amount of signals) was

typically about 10. The signal of the first arriving particle in the window is taken as a sample and assigned to the time moment of the window beginning. The shift between the sample time and the real time of the particle arrival (signal) causes a deviation of the registered velocity value from the real value corresponding to the beginning of the window. This can be a source of high-frequency noise in velocity spectra calculated from the quasi-equidistantly sampled time series. The velocity component statistics are not influenced by the deviations mentioned. When calculating cross-correlations between the velocity components, special measurements were carried out in the even-time coincident mode.

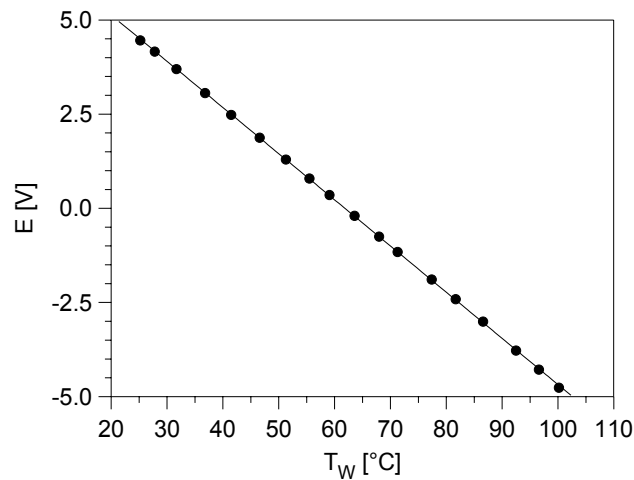


Figure 5. Calibration function of the temperature probe with platinum-plated tungsten wire.

2.2.2. Temperature Measurements

For the temperature measurements in the wind tunnel the resistance-wire technique is applied. The temperature probe is made up of a thin wire suspended between the tips of two prongs. When the probe is placed in the flow, the temperature of the ambient air can be determined from the temperature-dependent electrical resistance of the wire. The resistance-wire technique, which is a special branch of hot-wire anemometry, is described in detail in literature, see *e.g.* Sandborn [47], Strickert [51], Perry [39], Lomas [29], and Bruun [4].

In the IHW wind tunnel, the flow temperature is measured with a 2.5 μm -thick and 1.25 mm-long platinum-plated tungsten wire probe. Figure 5 presents a characteristic linear calibration function of the probe.

The electric current through the wire causes a spurious heating, which should be taken into account in the temperature measurements. The employed current of 1 mA leads to an excess temperature value of about 0.2 K.

In addition, the heat inertia of the wire must be accounted for in the measurement procedure. If the time constants of the wire and of the prongs are known, it is possible to compute the transfer function of the resistance-wire probe and correct the temperature time series for the inertia effects of the probe.

For the experimental determination of the time constant of the wire, its middle point was heated by a focused laser beam. The laser beam was switched on and off by means of a rotating disc, one half of which was transparent. The circular velocity of the disk was 4000 cycles per minute. The signal of the wire placed in a constant-velocity air flow was digitized with a temporal resolution of 40 KHz. In Fig. 6, the measured cooling rates of the wire corresponding to different flow velocities are shown. The time constant of the wire was evaluated as the period during which the temperature of the wire drops by the factor of e from its initial value.

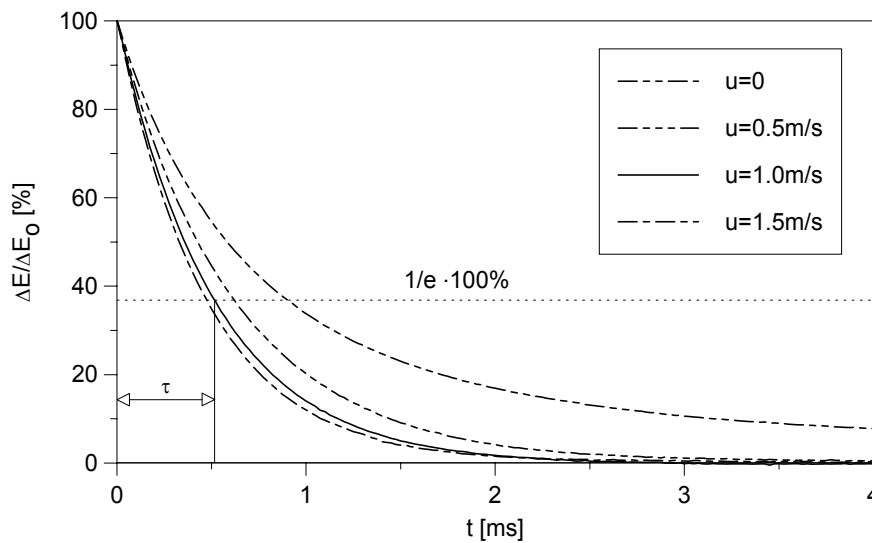


Figure 6. Cooling rate of the resistance wire.

TABLE 1. Time constants and cut-off frequencies of the platinum-plated tungsten wire ($d=2.5 \mu\text{m}$, $l=1.25 \text{ mm}$) experimentally determined at different flow velocities.

Flow velocity, m/s	Time constant, ms	Cut-off frequency, Hz
0	0.90	177
0.5	0.62	257
1.0	0.52	306
1.5	0.47	339

TABLE 2. Time constants and cut-off frequencies of the prongs experimentally determined at different flow velocities.

Flow velocity, m/s	Time constant, s	Cut-off frequency, Hz
0.5	5.09	0.03
1.0	1.10	0.14
1.5	0.85	0.19

The time constant of the prongs was estimated in a similar way. In this case, the whole probe was heated by means of a hot-air jet. After switching off the heating, the probe was exposed to a cold air flow and the cooling rate was measured. The time constant of the wire is several orders of magnitude smaller than that of the prongs. Therefore, the influence of the wire could be neglected while determining the cooling rate of the prongs.

The experimentally determined time constants of the wire and the prongs are listed in Tables 1 and 2 for different flow velocities.

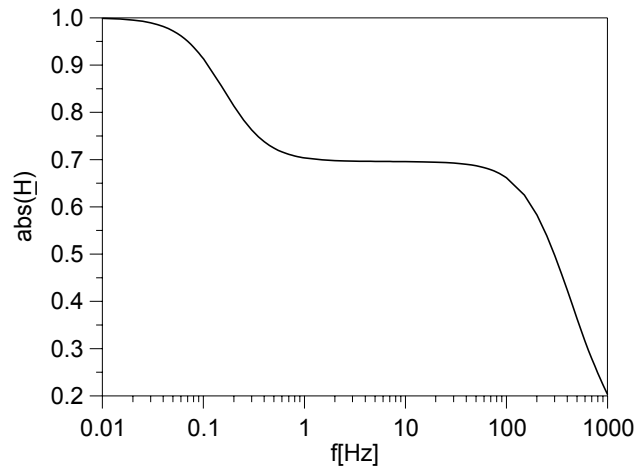


Figure 7. Transfer function of the resistance-wire probe computed with the experimentally determined time constants of the wire and of the prongs.

The transfer function of the temperature probe was calculated based on the experimentally determined time constants of the wire and the prongs. An empirical approach verified by Paranthoen *et al.* [38] was employed for the calculation. The calculated transfer function for flow velocity of 1 m/s is shown in Fig. 6. In the low-frequency range, this function exhibits the fast decay associated with the inertia of the prongs. Within the range of 1 Hz to 100 Hz, the transfer function passes through a plateaulike interval. With the frequency increasing beyond this interval, the shape of the transfer function is becomes closer to that of an infinitely long wire.

2.2.3. Parallel Velocity and Temperature Measurements

The width of the LDV even-time window is 0.01 s which provides a sampling frequency of 100 Hz. Each velocity time series includes values obtained in 16384 even-time windows. Thus, its length is 163.84 seconds.

Discretization of the analog signal of the resistance wire is triggered by the LDV signal in order to synchronize the velocity and temperature time series. In this way, the temperature time series have the same length as the velocity time series. The temperature probe is placed at the same level as the LDV measuring volume, and shifted 1 mm downstream. This shift desynchronizes velocity and temperature measurements at frequencies of 1000 Hz and more, (the typical mean-flow velocity in the tunnel is 1 m/s). As will be seen from the spectra shown

in section 3.3, at such frequencies the energy of both velocity and temperature turbulent fluctuations is small compared with the energy in the resolved frequency range. Therefore, the velocity and temperature measurements in the tunnel can be regarded as coincident in time and space.

2.2.4. Flow Visualization

The laser light sheet technique is employed to visualize flow and turbulence structure in the wind tunnel. An argon-ion laser is used as the source of light. The laser beam is embedded into a multimode glass fiber of 25-mm diameter. From the exit of the fiber the beam passes through a spherical biconvex lens of 10-mm focal length. The lens provides a divergent light bunch beyond the focal point of the lens. An additional convex cylindrical lens of 80-mm focal length is used to bundle up the bunch in the horizontal plane while in the vertical it is kept divergent. As a result, a light sheet is generated in front of the lens system. The distance between the sheet and the lenses may be varied in the range of 1 m to 7 m depending on the disposition of the lenses. The typical thickness of the light sheet is about 1 cm, and its height is about 1 m.

A white 1,2-propyleneglycol fog is used as the visualizing material. It is admixed into the lowest layer at the test section inlet. Buoyant thermals rising from the heated floor of the tunnel are thus colored white. They are clearly seen in the light sheet against the background of more transparent air entrained down from the upper layers of the flow.

The visualized flow patterns are captured by a television camera and recorded on a video tape. Afterwards, typical flow patterns are selected from the tape and digitized for further image processing.

3. Model Results

3.1. CBL DEVELOPMENT IN THE WIND TUNNEL

3.1.1. Evolution of Temperature and Turbulence Fields

The inlet velocity, and temperature profiles corresponding to the basic experimental setup of the present study are schematically shown in Fig. 8. The velocity is held constant in the vertical with a value of 1 m/s. The temperature is constant (20°C) over the two lower layers, 30-cm deep in total. Between the second and the third layer, a temperature jump of 30°C is imposed. Above the jump, the temperature is grows with height at a rate of 67°C/m. The heat flux of 1250 W/m² through the floor of the tunnel is kept constant in the horizontal. The presented experimental configuration differs slightly from the one considered in Fedorovich *et al.* [15], where the CBL case with a weaker stratification (33°C/m) above the inversion was investigated.

Measurements of the flow parameters in the tunnel are carried out at five fixed locations corresponding to the positions of the windows, through which the laser light penetrates in the tunnel. If the origin of the coordinate system is placed at the floor midpoint near the test section inlet, and the x axis is oriented parallel to the flow, then the measurement locations (windows) are found at $x=0.68$ m (I window), $x=2.33$ m (II window), $x=3.98$ m (III window), $x=5.63$ m (IV window), and $x=7.28$ m (V window). Accordingly, the y axis is oriented perpendicular to the flow, and the z axis is directed upwards. All measurement data presented in this section refer to the central longitudinal plane of the tunnel.

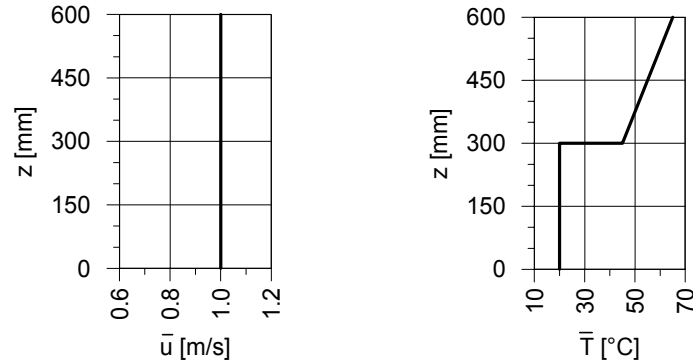


Figure 8. Idealized velocity and temperature profiles at the test section inlet.

The evolution of the mean temperature field in the tunnel is shown in Fig. 9. Corresponding changes of the turbulence field can be seen in Fig. 10. At the first measurement location, $x=0.68$ m, the shape of temperature profile is quite similar to that of the inlet profile, see Fig. 8. Beyond the unstably stratified near-surface region occupying roughly one quarter of the depth of the initially neutrally stratified layer, the changes in the temperature field are not significant. In the unstable region, fluctuations of both plotted velocity components are exaggerated due to the turbulence production by buoyancy forces. However, the resulting turbulent exchange is not strong enough to mix up the air near the surface. The vertical velocity excess in the turbulized region vanishes towards the surface due to the damping effect of the surface on the vertical turbulent motions.

While the flow proceeds further over the heated floor of the tunnel, the depth of the zone warmed by the convective heat transfer from the surface increases. At $x=2.33$ m, only the uppermost portion of the initial neutral layer preserves its original temperature. The turbulence intensity in the heated region is markedly higher than at $x=0.68$ m, whereas the overall temperature lapse rate is smaller due to the stronger mixing. The surface velocity shear also contributes to the intensification of turbulent exchange and to the transport of heat upwards. The beginning of temperature inversion erosion can be identified in the temperature profile at $x=2.33$ m. It is nevertheless clear that at this stage of flow evolution the turbulence is not developed enough to provide a strong turbulent mixing typical for the atmospheric CBL.

Over the range of distances between $x=2.33$ m and $x=3.98$ m, the temperature profile drastically changes its shape. The kneelike minimum in the profile under the capping inversion at $x=2.33$ m is replaced in the profile at $x=3.98$ m by much higher temperature values, which grow with height. This comparatively rapid heating of the flow in the under-inversion region is caused by two main mechanisms: (i) heat transport upwards from the surface by strong convective motions, (note turbulence intensities at $x=2.33$ m and at $x=3.98$ m in Fig. 10), and (ii) downward transport of heat from the warm region above the inversion due to entrainment. The latter is maintained by convective thermals, which are sufficiently developed at $x=3.98$ m and thus capable of overshooting in the stably stratified environment above the inversion. The increase of the turbulence intensity within the range of fetches from $x=2.33$ m to $x=3.98$ m is associated with the release of potential energy accumulated in the unstable sublayer below the

inversion with a superadiabatic temperature gradient. This potential energy is transformed into the kinetic energy of turbulent fluctuations when the under-inversion layer overturns, (see the temperature profile transformation from $x=2.33$ m to $x=3.98$ m in Fig. 9).

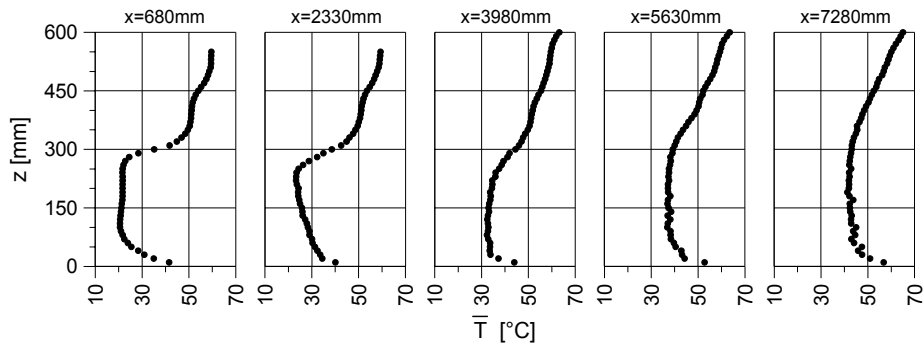


Figure 9. Evolution of the mean-temperature field along the tunnel.

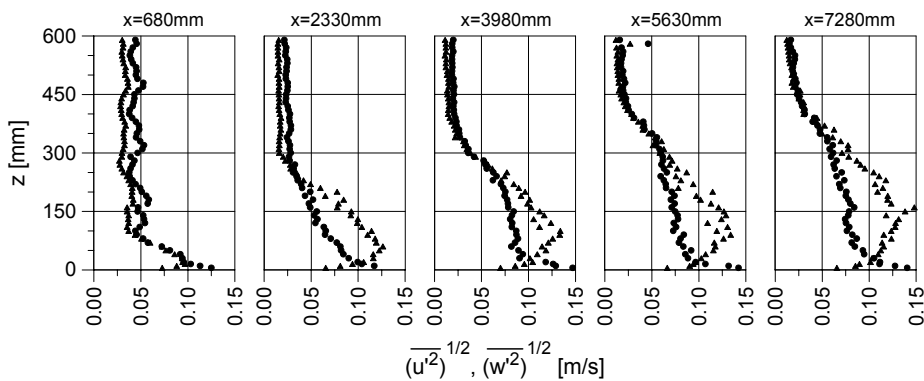


Figure 10. Development of turbulence along the tunnel. Dots: u fluctuations, triangles: w fluctuations.

As a result of the above processes, the convectively mixed layer is formed in the lower portion of the wind tunnel flow.

Downstream from $x=3.98$ m, at $x=5.63$ m and at $x=7.28$ m, the mean-flow temperature profile retains the shape characteristic of the developed atmospheric CBL: a sharp decrease of temperature in the near-surface layer; an approximate thermal uniformity within the mixed layer; a temperature increase with height across the inversion; and a quiescence of temperature field in the stably stratified flow aloft. The CBL depth, which can be roughly estimated from the elevation of the capping inversion midpoint in Fig. 9, and also from the vertical extension of the turbulized zone in Fig. 10, increases progressively with distance. This growth is accompanied by cooling of the stably stratified layer due to the entrainment of warmer air from above the inversion into the bulk of the mixed layer.

3.1.2. Visualization of Turbulence Structure

In Fig. 11, a visualized flow pattern over the central longitudinal plane of the tunnel is presented. The fog in the plot is colored black. Large towerlike convective structures (thermals) transporting the fog upwards are clearly seen over the whole range of distances shown. The vertical dimensions of the thermals increase downwind. The CBL growth rate along the tunnel can be estimated from longitudinal changes of the heights of thermals. This rate is about 5 cm per 1 m length. The thermals penetrate deeply into the stably stratified outer flow region. Their diameters decrease with height. This is also a feature of thermals observed in the atmospheric CBL (Hooper and Eloranta [20]).

The maximum height of thermals in the simulated CBL is about 0.5 m. According to Nelson *et al.* [34], this height can be taken as the upper edge of the entrainment zone, and hence as the CBL top. A typical horizontal scale of rising thermals is approximately 0.2 m. The downdrafts may be identified in the plot as lighter colored areas. They are typically twice as wide as the thermals. Proportions between the horizontal scales of updrafts and downdrafts in the wind tunnel CBL correspond well to atmospheric observations by Lenschow and Stephens [27]. The upper parts of the wind tunnel thermals do not display a significant sideward transport of air from the thermals at the capping inversion level.

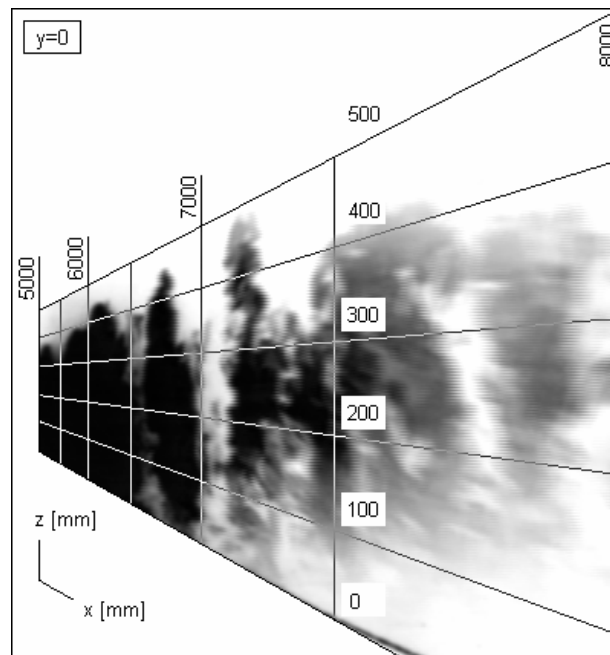


Figure 11. Light sheet image of the CBL turbulence structure along the central longitudinal plane of the tunnel.

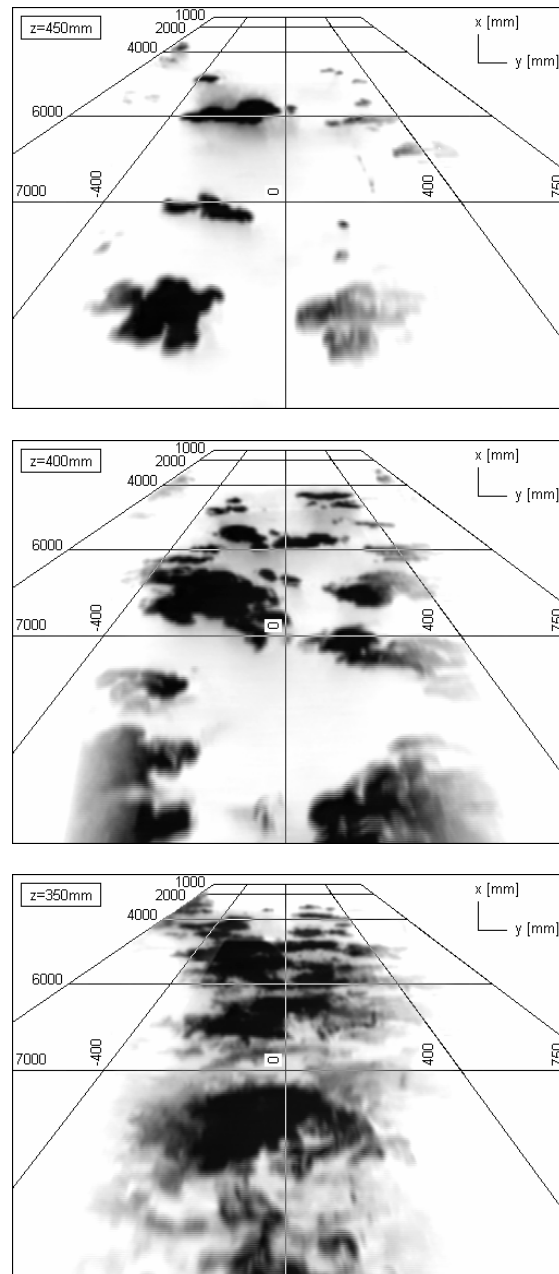


Figure 12. Changes of turbulence structure throughout the upper portion of the CBL. The lowest light sheet image refers to the lowest registration plane.

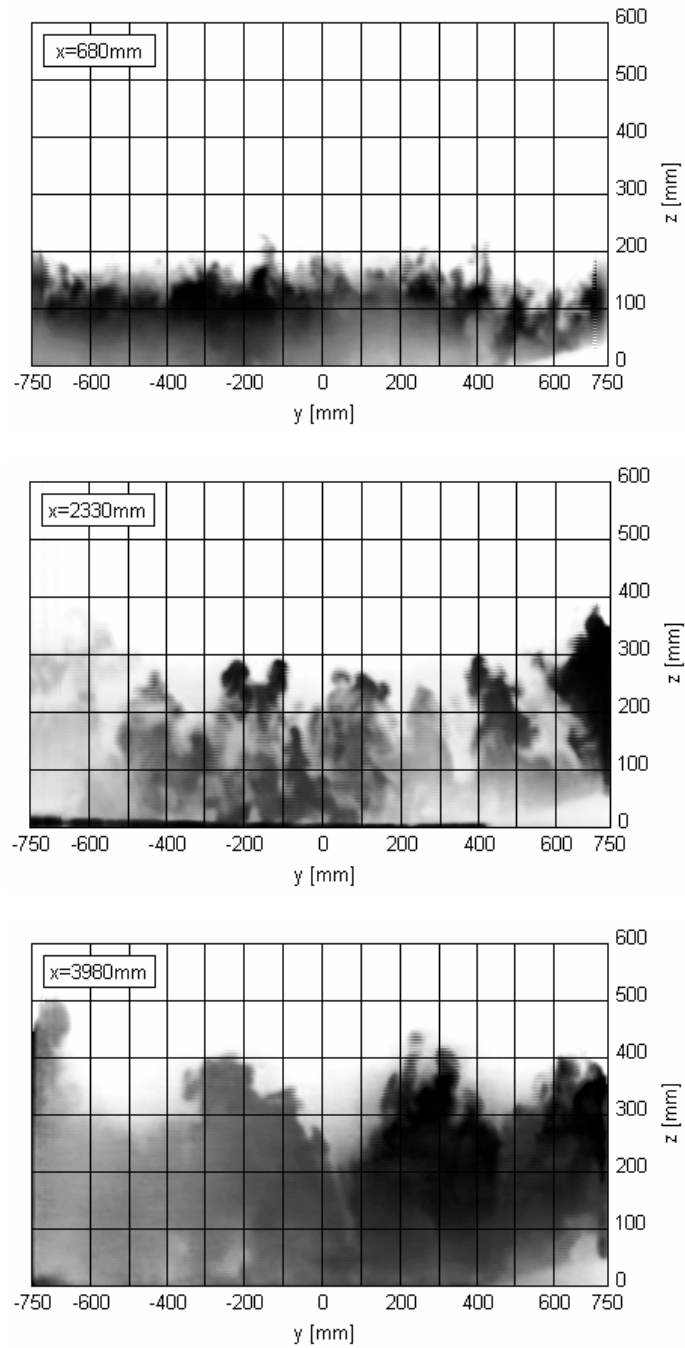


Figure 13. Light sheet images of the CBL turbulence structure perpendicular to the wind tunnel flow.

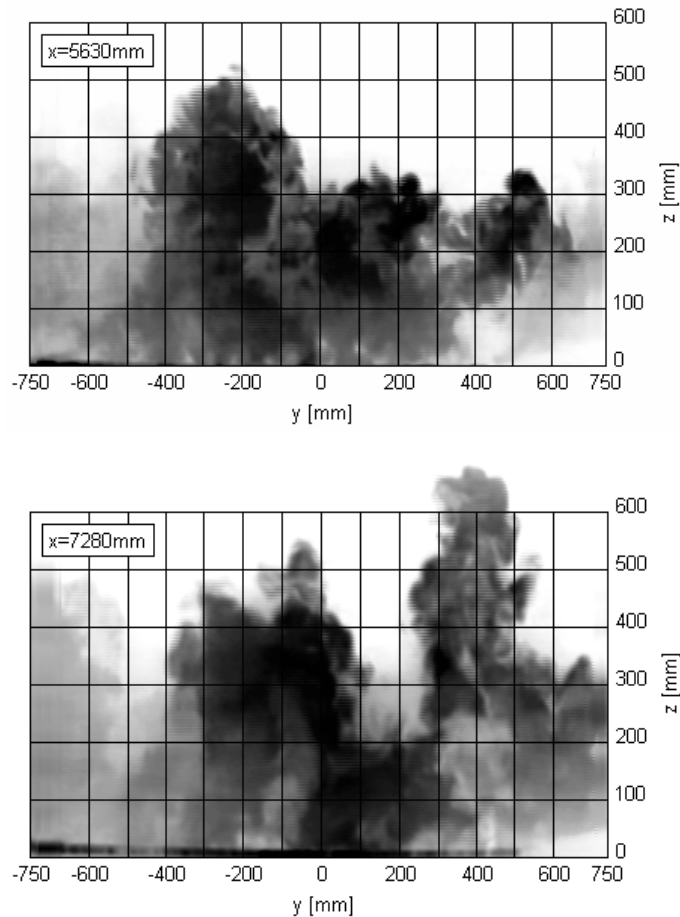


Figure 13 (continued). Light sheet images of the CBL turbulence structure perpendicular to the wind tunnel flow.

The visualized patterns presented in Fig. 12 display the changes of turbulence structure in the vicinity of the capping inversion. As can be inferred from the temperature plots in Fig. 9, the inversion elevation within the fetch range of 4 m to 7 m changes from 0.35 m to 0.45 m. The patterns in Fig. 12 visualize three flow slices at different heights within the inversion layer. At $z=0.35$ m, which is at the lower edge of the inversion layer, large-scale turbulence structures are dominant in the flow. The turbulence pattern at the next level, $z=0.40$ m, which is in the core of the inversion layer, is much more patchy. Typical sizes of rising thermals here are smaller than under the inversion. At the highest elevation shown, $z=0.45$ m, the tops of only a few thermals are observed which appear as black spots on the background of white ambient air. The shape of these spots indicates that the horizontal cross-sections of the thermals are rugged due to the lateral entrainment of surrounding air inside the thermals.

Light sheet images of the flow in the cross-sections corresponding to the measurement windows are presented in Fig. 13. At the first location, $x=0.68$ m, small buoyant plumes rising

from the heated floor into the neutrally stratified environment are clearly seen. They are too small to reach the inversion base. At $x=2.33$ m, the size of the plumes increases, but only a few of the plumes extend up to the inversion, which blocks them. Peculiar fine-structure convective elements, which look like fingers, can be observed at the tops of the plumes.

Further development of the turbulence regime in the tunnel is associated with a merging of plumes into the buoyant thermals, which are bigger and stronger turbulence structures than the plumes. Larger-scale thermals are well seen in the plots corresponding to $x=3.98$ m, $x=5.63$ m, and $x=7.28$ m. The thermals penetrate far into the stably stratified flow above the inversion. Their horizontal dimensions typically decrease with height which is consistent with our previous observations of thermals in Figs. 11 and 12. It is remarkable that the upper portions of some thermals are composed of fingerlike buoyant elements similar to the tops of convective plumes at the earlier stages of the CBL development. These fingers penetrate into the stably stratified flow ahead of a thermal itself.

3.1.3. Stages of CBL Evolution

Departing from temperature and turbulence evolution patterns, examples of which are shown in Figs. 9 and 10, and based on the analysis of visualized flow patterns, (see Figs. 11 - 13), a subdivision of the CBL evolution into stages can be suggested. This subdivision is schematized in Fig. 14.

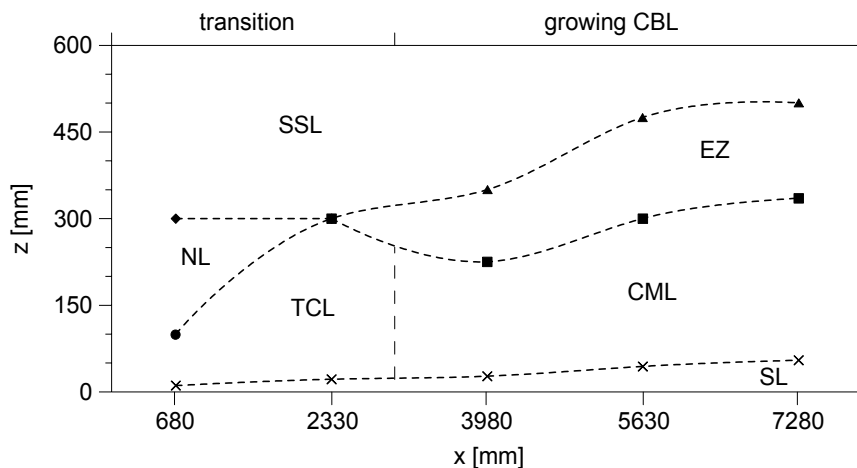


Figure 14. Development of the CBL in the wind tunnel. Abbreviations: SSL – stably stratified layer, EZ – entrainment zone, NL – neutrally stratified layer, TCL – transitional convective layer, CML – convectively mixed layer, and SL – surface layer.

The transitional convective region is located within the first three meters of the test section length. Throughout this region, the adjustment of the preshaped flow to the bottom-up buoyant and shear forcings takes place. The transitional convective boundary layer grows on the background of the neutrally stratified flow. The depth of this layer is determined by the average height of convective plumes growing into the neutral layer. The overall temperature gradient in the transitional convective layer is superadiabatic. After buoyant plumes rising from the heated surface reach the inversion base, the convectively mixed layer develops within a comparatively

short range of fetches. Turbulence pattern in this layer is primarily constituted of the convective thermals (warm updrafts) and the associated cold downdrafts, which both are stronger and larger convective structures than plumes in the transitional convective layer.

Above the convectively mixed layer, the interfacial layer (entrainment zone) is formed. The intermittent turbulence structure in this layer is composed of penetrating thermals, whose horizontal dimensions decrease with height, and of wide downdrafts transporting warm air down from the outer flow region. Due to the entrainment mechanism, the CBL progressively grows along the tunnel. The typical depth of the entrainment layer in the wind tunnel flow is from one quarter to one third of the total CBL depth.

Across the comparatively shallow surface layer adjacent to the heated floor, the mean-flow temperature and velocity characteristics sharply change with height from their near-wall values (zero for velocity) to the mixed-layer values.

TABLE 3. Integral parameters of the simulated CBL.

Fetch, m	3.98	5.63	7.28
z_i , m	0.30	0.35	0.40
w_* , m/s	0.163	0.185	0.198
T_* , K	3.86	4.32	4.45

TABLE 4. Dimensionless characteristics of the simulated CBL.

Fetch, m	3.98	5.63	7.28
$Ri_{\Delta T}$	3.9	3.0	2.5
Ri_N	5.2	5.4	6.0
u_* / w_*	0.43	0.38	0.35

In Tables 3 and 4, integral parameters of the convective regime and values of dimensionless combinations corresponding to three measurement locations within the developed CBL are given. The Deardorff [8] convective temperature scale T_* in Table 3 is defined as $T_* = Q_s / w_*$. The CBL depth scale z_i is determined from the elevation of the heat flux minimum within the entrainment zone.

3.2. RESULTS OF TURBULENCE MEASUREMENTS

3.2.1. Turbulence Statistics

Dimensionless profiles of turbulence statistics in the wind tunnel CBL are shown in Figs. 15 - 17. Hereafter, we shall exclusively consider data obtained at $x \geq 3.98$ m which thus refer to the stage of the developed CBL. The plotted statistics are normalized with the traditional Deardorff [8] convective scales: z_i for the height, w_* for the velocity, and T_* for

the temperature. Despite the well-known limitations, (discussed, for instance, in Wyngaard [58]), the Deardorff mixed-layer scaling presents a convenient common background for the comparison of measurement and model results from different CBL studies. Some of these results are shown in Figs. 15 - 17.

The heat flux profiles are presented in Fig. 15a. In the interfacial layer, the negative heat flux of entrainment from the wind tunnel model is much smaller compared to the negative Q values from the other studies. The weaker inversion in the wind tunnel CBL leads to the smaller magnitude of temperature fluctuations in the interfacial layer. In the water tank and large eddy simulation (LES) studies, data from which we consider for comparison, the characteristic values of $Ri_{\Delta T}$ and Ri_N were respectively 15 and 150 (Deardorff and Willis [9]), and 25 and 100 (Schmidt and Schumann [48]).

The effects of capping inversion and stable stratification in the outer flow are most vividly displayed in the normalized profiles of the temperature fluctuations (Fig. 15b). In the lower portion of the CBL, where the turbulence regime is mainly governed by bottom-up forcings, all data sources provide similar values of the temperature variance. The variances from the wind tunnel experiments are smallest near the CBL top, where water tank and LES studies with stronger stabilities inside and above the inversion layer predict much higher values of the normalized temperature variance.

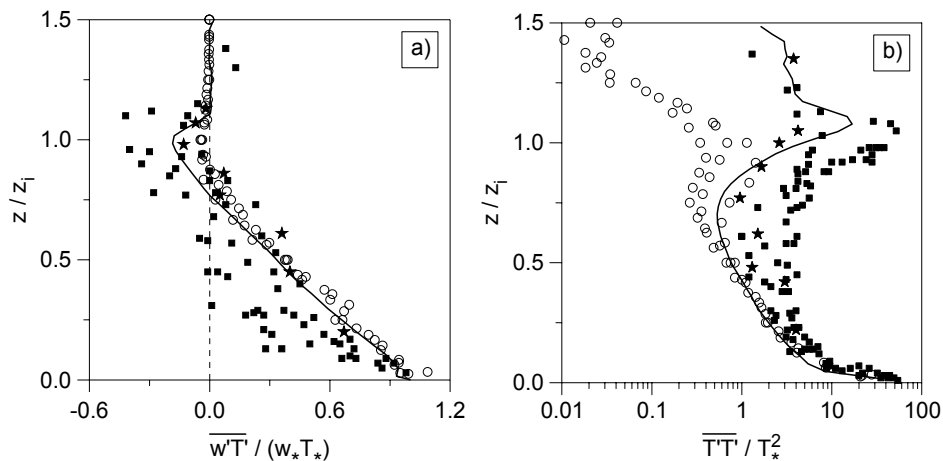


Figure 15. The vertical turbulent heat flux (a) and the temperature variance (b) in the CBL. The wind tunnel data (circles) are compared with the results of atmospheric measurements (Caughey and Palmer [5], and Lenschow *et al.* [28]), squares; water tank simulations (Deardorff and Willis [9]), stars; and LES (Schmidt and Schumann [48]), lines.

The divergence of $\overline{u'u'}$ data from the different sources in Fig. 16a is rather large. There are indications (Schmidt and Schumann [48]) that the water tank simulations of Deardorff and Willis [9] and the atmospheric measurements of Caughey and Palmer [5], which both give rather high $\overline{u'u'}$ values, were affected by horizontal variations of the surface heat flux in the first case, and by wind shear in the second. Surface velocity shear in the wind tunnel CBL leads to the enhancement of horizontal velocity variance in the lower portion of the CBL. The

turbulence enhancement in the downwind region of the transition zone, at $x=3.98$ m (see section 3.1.1), is represented in the plot by the group of wind tunnel data points shifted to the right from the main profile.

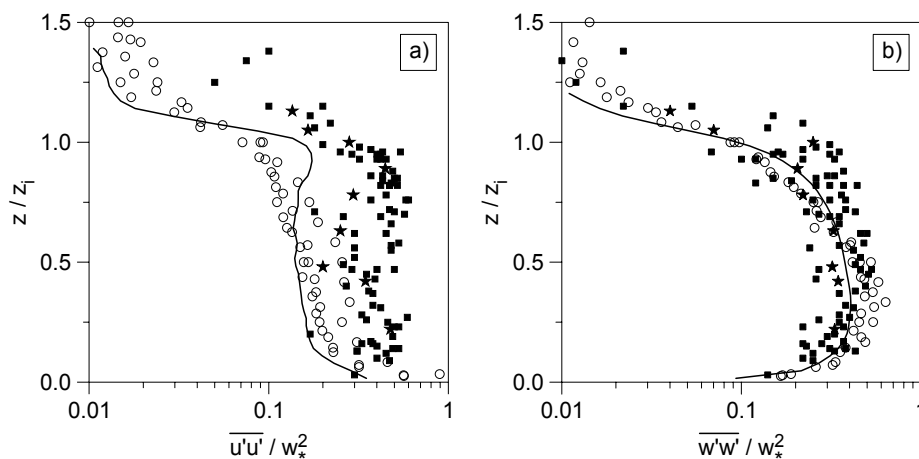


Figure 16. Variances of the longitudinal (a) and vertical (b) velocity components in the CBL. The notation is the same as in Fig. 15.

Two main mechanisms are presumably responsible for the enhancement of the longitudinal velocity fluctuations near the CBL top. The first is the sideward transport of air from the thermals in the inversion layer. This is an explanation for the marked maxima in the $\overline{u'u'}$ profiles from the water tank and LES studies with the relatively strong capping inversions. The wind tunnel data obtained in the CBL with a weak capping inversion merely give a slope change (bend) in the $\overline{u'u'}$ profile at $z/z_i \approx 1$. This points to a strong correlation between the magnitude of the $\overline{u'u'}$ variance in the upper portion of CBL and the inversion strength. The second mechanism of the $\overline{u'u'}$ enhancement at $z/z_i \approx 1$ is associated with the velocity shear across the inversion layer. Such an elevated shear may be one of the reasons for the large $\overline{u'u'}$ variance values in the upper part of the atmospheric CBL.

Figure 16a suggests one more conclusion: with a stronger damping effect of the buoyancy force above the inversion (larger Ri_N , see the water tank and LES data in the plot), the horizontal velocity variance in the upper portion of the CBL decays faster with height than in the wind tunnel case of small Ri_N .

Within the main portion of the CBL, the wind tunnel data on $\overline{w'w'}$ (Fig. 16b) are in fair agreement with the water tank, atmospheric measurements, and the LES results. Still, the $\overline{w'w'}$ variances obtained in the wind tunnel at $z/z_i < 0.5$ are slightly larger than the variances from the other studies. Like in the case of the $\overline{u'u'}$ variance, the enhancement of $\overline{w'w'}$ in the wind tunnel flow can be caused by the surface shear and, at $x=3.98$ m, by the transition effects. Additionally, the vertical velocity fluctuations in the core of the wind tunnel CBL may be

exaggerated due to weak quasi-stationary cellular circulations, which are discussed in Fedorovich *et al.* [15]. The behavior of $\overline{w'w'}$ at $z/z_i > 1$ is analogous to that of $\overline{u'u'}$: with larger Ri_N (e.g. in the LES experiments) the decay of the velocity variance with height is steeper.

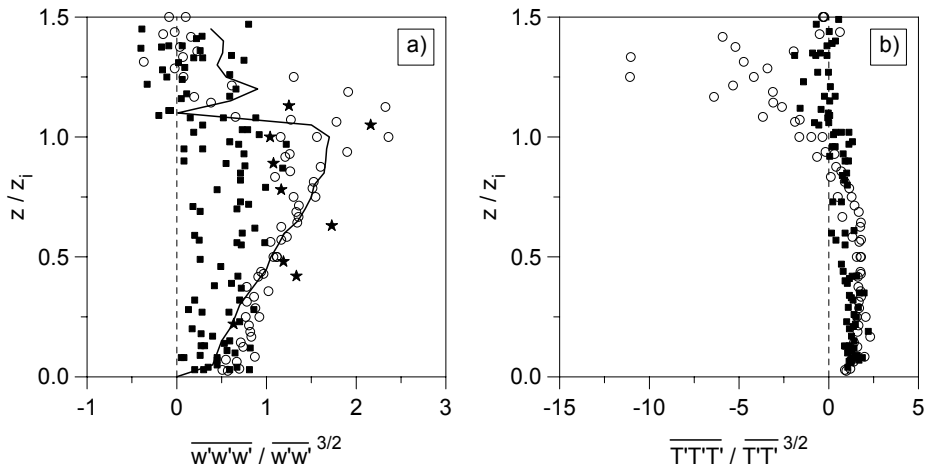


Figure 17. Skewness of (a) vertical velocity and (b) temperature in the CBL. The wind tunnel data (circles) are compared with the results of atmospheric measurements (Sorbjan [50]), squares; water tank simulations (Deardorff and Willis [9]), stars; and LES (Schmidt and Schumann [48]), line.

Vertical distributions of the vertical velocity and temperature fluctuation skewness are shown in Fig. 17. The wind tunnel data on the temperature skewness are compared only with the atmospheric measurements.

Positive values of the vertical velocity skewness in the upper portion of the CBL reveal a wider range of values occupied by updrafts (positive w') than by downdrafts (negative w'). The skewness observed in the atmosphere varies only slightly in the vertical, contrary to the wind tunnel, water tank and LES data, which clearly indicate the growth of skewness with height in the main portion of the layer. Narrow buoyant fingerlike elements rising from the tops of the thermals in the simulated CBL may be the main cause of the large skewness values from the wind tunnel. We have observed these elements in the visualized flow patterns, see section 3.1.2.

Distinctions between the atmospheric and wind tunnel data on the temperature skewness (Fig. 17b) are large inside and above the inversion layer, where the regime of temperature fluctuations is essentially determined by the thermals penetrating into the stably stratified environment. Comparatively narrow and cool thermals in the wind tunnel CBL provide more asymmetric distribution of temperature fluctuations and thus larger negative values of the temperature skewness at $z/z_i \geq 1$.

3.2.2. Turbulence Kinetic Energy Budget

We consider the turbulence kinetic energy (TKE) balance in a quasi-stationary CBL, which slowly evolves in the x direction and which is quasi-homogeneous in the y direction (Stull [52]):

$$\underbrace{\bar{u} \frac{\partial e_k}{\partial x} + \bar{w} \frac{\partial e_k}{\partial z}}_{\text{advection}} = \underbrace{-\overline{u'w'}}_{\text{shear production}} \frac{\partial \bar{u}}{\partial z} + \underbrace{\frac{g}{T_0} \overline{w'T'}}_{\text{buoyant production}} - \underbrace{\frac{1}{\rho_0} \frac{\partial \overline{p'w'}}{\partial z}}_{\text{pressure correlation}} - \underbrace{\frac{\partial \overline{e_k w'}}{\partial z}}_{\text{turbulent diffusion}} - \varepsilon = 0, \quad (2)$$

where $e_k = 0.5(u'^2 + v'^2 + w'^2)$ stands for the turbulence kinetic energy; p is the pressure; g is the acceleration due to gravity; the ensemble (Reynolds) averages are denoted by overbars; the primes signify turbulent fluctuations; T_0 and ρ_0 are reference values of temperature T and density ρ , respectively. The TKE integral budget in the wind tunnel CBL was evaluated and analyzed in Fedorovich *et al.* [15].

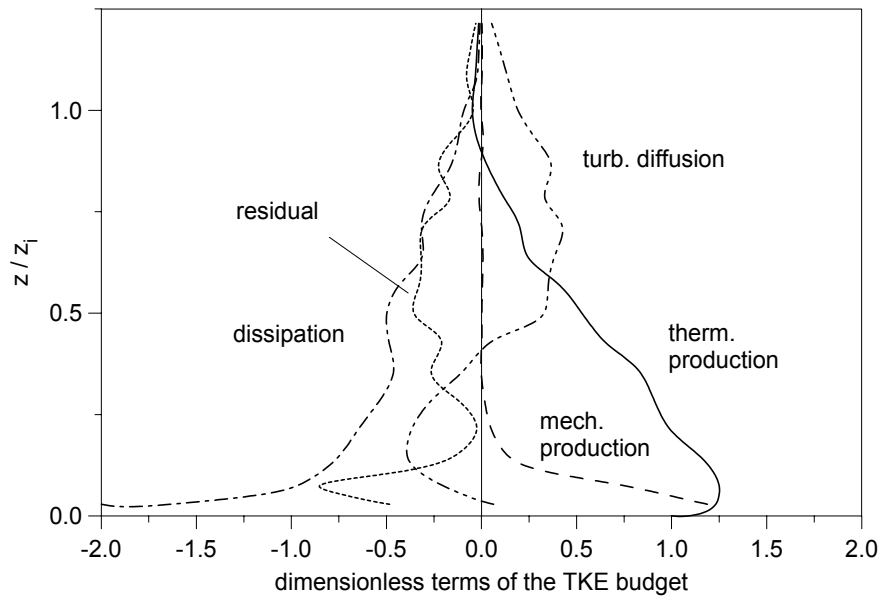


Figure 18. Normalized components of the TKE budget in the wind tunnel CBL.

Only two components of velocity can be simultaneously registered by the LDV system employed for velocity measurements in the tunnel. According to a regular measurement program, these are the longitudinal (u) and vertical (w) velocity components. Special measurements performed for the estimation of the transversal velocity component v have shown that v'^2 values are typically very weakly correlated with w' . The estimate $-\partial \overline{e_k w'} / \partial z = -0.5(\partial \overline{u'^2 w'} / \partial z + \partial \overline{w'^3} / \partial z)$ has been employed for the evaluation of TKE turbulent diffusion

from the velocity time series. The pressure correlation term has not been calculated due to the absence of data on pressure fluctuations in the simulated CBL. The advection term has also been omitted due to the inability of determining it accurately from the wind tunnel data. We may expect, however, that it is a comparatively small component of the TKE balance in the wind tunnel (Fedorovich *et al.* [15]). The TKE dissipation rate ε was determined from the velocity spectra (the procedure is described in section 3.3.3). The shear and buoyancy production terms were directly evaluated from the measured data.

The TKE balance in the wind tunnel flow at $x=5.63$ m is presented in Fig. 18. Before being plotted, the balance components were normalized by w_*^3 / z_i . The residual term represents the net contribution to the TKE balance by advection, pressure transport, and other smaller terms omitted in the budget considerations.

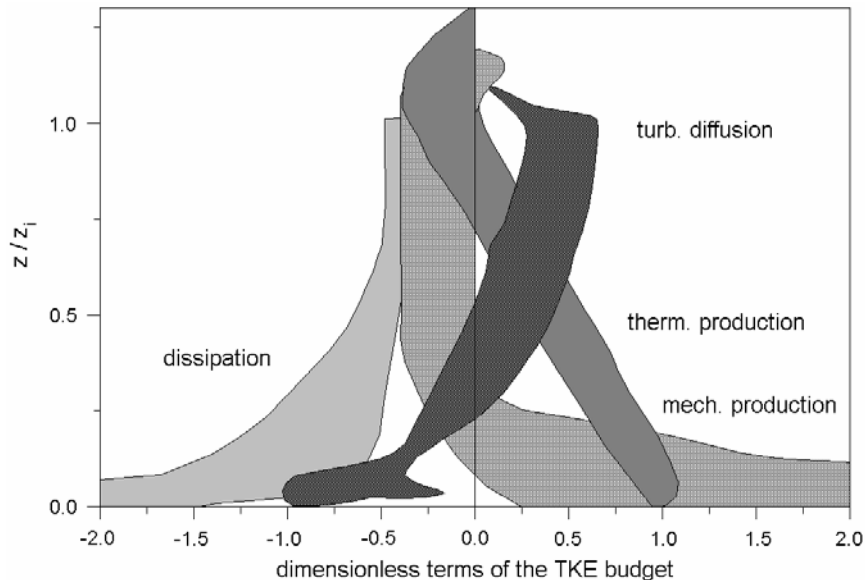


Figure 19. The TKE budget in the CBL. The shaded areas indicate ranges of values obtained by merging data from different experimental and model sources, after Stull [52].

The mechanical (shear) production of the TKE is maximum near the surface, where it exceeds even the thermal (buoyant) production. The total TKE production in the lower portion of the CBL is compensated largely by high TKE dissipation rate. Also, some energy is extracted from this flow region due to the TKE turbulent transport (diffusion) upwards. The transport term changes its sign slightly below the CBL middle. In the upper portion of the layer, the TKE grows at the expense of the energy diffusion from below. Across the lower third of the CBL, the TKE shear production steeply drops to very small values, and remains close to zero up to the CBL top. The thermal production gradually decays with height throughout the main portion of the CBL. The proportion between the mechanical and buoyant TKE production terms shows that buoyant production is dominant in the bulk of the wind tunnel CBL. Close to

the CBL top, the thermal production of the TKE is negative within a certain range of heights due to the heat exchange across the capping inversion.

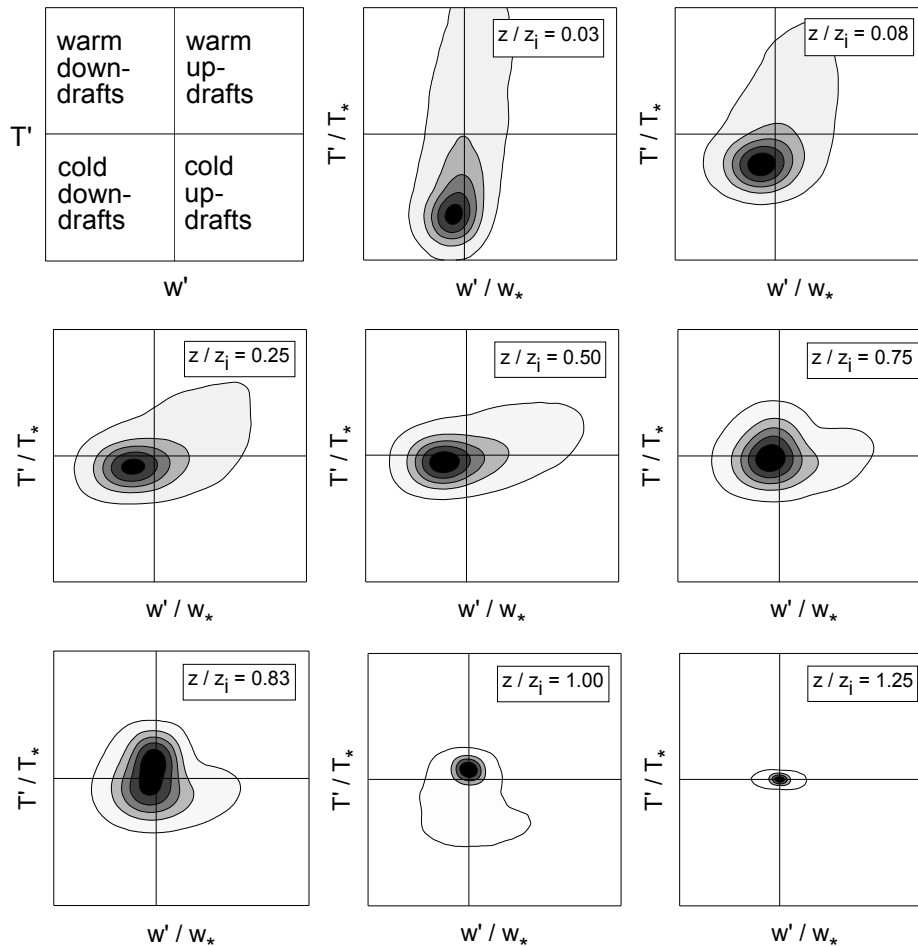


Figure 20. Joint probability density distribution of the vertical velocity and temperature fluctuations at different elevations in the wind tunnel CBL at $x=3.98$ m.

Figure 19 presents the normalized components of the TKE balance compiled from a variety of experimental and model studies of the atmospheric CBL. The comparison with Fig. 18 certifies that the TKE balance components in the simulated CBL are well within the range of values provided by other data sources.

3.2.3. Probability Density Distributions

Joint probability density distributions of the vertical velocity and temperature fluctuations shown in Fig. 20 provide information about the statistical structure of the vertical heat transport by convective motions. The four quadrants of the distribution base (the plot in the upper left

corner of Fig. 20) can be related to the warm and cold up- and downdrafts, which constitute the internal turbulence pattern of the CBL, (see the visualized flow images in section 3.1.2).

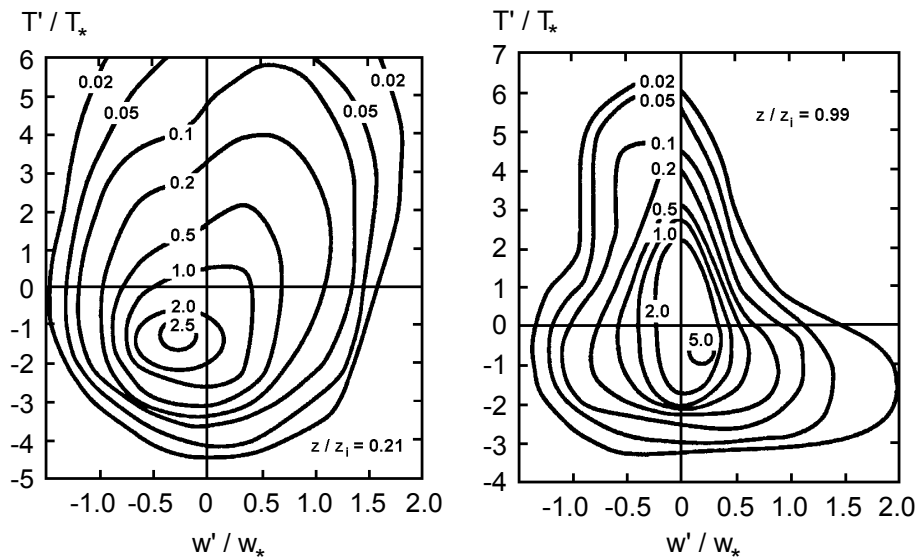


Figure 21. Joint probability density distributions of the vertical velocity and temperature fluctuations at two dimensionless elevations in the water tank CBL model of Deardorff and Willis [9].

At the lowest elevation shown ($z / z_i = 0.03$), which is located inside the convective surface layer, the joint distribution provides evidence of strong vertical turbulent heat flux and large, positively skewed temperature fluctuations. Whilst the height increases within the range of 0.08 to 0.5, the temperature fluctuation magnitude decreases and the magnitude of the vertical velocity fluctuations increases, (see also Figs. 15b and 16b). This is the reason for the clockwise turn of the distribution pattern. From the probability distributions referring to the lower half of the CBL one can deduce that the vertical heat transport in this flow region is maintained mainly by hot updrafts and cold downdrafts. In the upper half of the convectively mixed layer, at $z / z_i = 0.75$ -0.83, the updrafts become cooler while the probability of warm downdrafts transporting hot air from the region above the inversion into the mixed layer increases. Inside the inversion layer, at $z / z_i = 1.00$, a characteristic bulge in the distribution pattern may be noted which is caused by relatively cold updrafts penetrating in the stably stratified layer. The pattern also gives an impression that these updrafts do not mix with the ambient warm air, but merely sink back into the convectively mixed layer as cool downdrafts. This observation is consistent with the previously discussed smallness of the heat flux of entrainment in the simulated CBL. At the upper edge of the inversion layer ($z / z_i = 1.25$), the distribution shows almost no correlation between w and T fluctuations. This is a sign of rather weak turbulent heat transport in this portion of the flow.

The joint probability patterns shown in Fig. 20 can be compared with their counterparts from the water tank study of Deardorff and Willis [9], see Fig. 21. In the lower portion of the CBL, at $z/z_i=0.21$, the probability pattern from the water tank reveals joint skewness of the velocity and temperature fluctuations associated with the upward heat transport by the thermals. The shape of the pattern is quite similar to that of the probability distribution from the wind tunnel model at $z/z_i=0.25$. Like the probability pattern from the wind tunnel CBL at $z/z_i=0.83$, the water tank distribution at $z/z_i=0.99$ exhibits asymmetry associated with the entrainment flux. Such asymmetry has been also observed by Mahrt and Paumier [30] in the probability pattern derived from measurements in the atmospheric CBL.

3.2.3. Conditional Sampling

Further information on the convective turbulence structure in the wind tunnel can be obtained through conditional sampling of the measured velocity and temperature time series. The updraft/downdraft conditional sampling implies sorting data from the time series into categories according to a selection criterion based on the sign and magnitude of the vertical velocity fluctuations. These categories are defined by the so-called indicator functions (Stull [52]). The indicator functions impose the thresholds which must be passed by an indicator variable (w' in our case) in order to be attributed to a particular category.

TABLE 5. Parameters of indicator function I (IF I).

Threshold for w'	
Updraft	$0 \leq w'$
Downdraft	$w' < 0$

TABLE 6. Parameters of indicator function II (IF II).

	Threshold for w'	Threshold for L_x
Updraft	$0.04\text{m/s} < w'$	$0.04\text{m} < L_x$
Environment	$ w' \leq 0.04\text{m/s}$	$L_x \leq 0.04\text{m}$
Downdraft	$w' < -0.04\text{m/s}$	$0.04\text{m} < L_x$

A time interval within which w' keeps a value beyond the threshold may be used as an additional selection criterion. This time interval can be expressed in terms of the horizontal length L_x of a rising / descending portion of the air, provided the mean longitudinal velocity of the flow is known. Using both the magnitude and the duration (length) criteria, the data points in the time series can be sorted into updraft and downdraft categories and then separately analyzed. Data that do not belong to any of the imposed categories may be associated with the environment embedding the ascending and descending motions.

Table 5 presents the parameters of the first indicator function (IF I) employed for conditional sampling. This indicator function merely distinguishes between upward and downward motions. The second indicator function (IF II), which parameters are given in Table 6, attributes some of the data points to the category of environment.

As seen from the examples of conditional sampling applied to the vertical turbulent heat flux and longitudinal velocity, (Fig. 22a and Fig. 22b, respectively), the sampling results are quite sensitive to the indicator function employed. With the imposed thresholds for the magnitude and size of upward / downward motions, the features of turbulent transport generally become more pronounced.

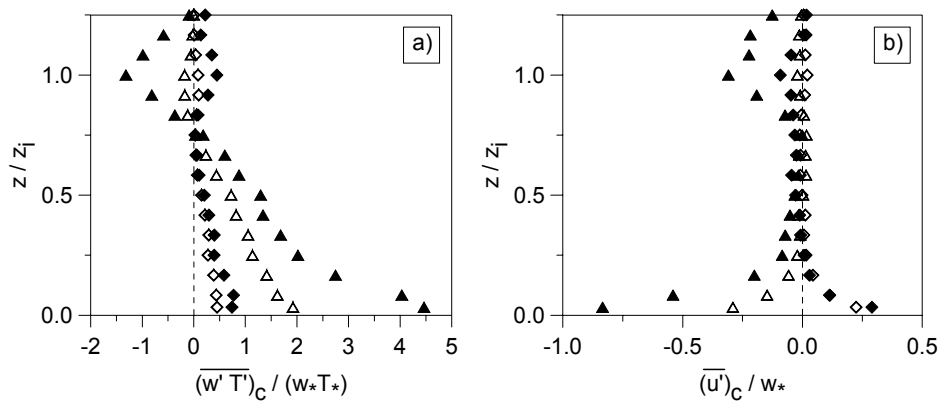


Figure 22. Conditionally sampled values of (a) vertical turbulent heat flux and (b) longitudinal velocity in the wind tunnel CBL at $x=3.98$ m. Open symbols: IF I; filled symbols: IF II. Triangles: updrafts; rhombi: downdrafts.

It may be concluded from Fig. 22a that in the lower portion of the CBL the heat is mainly transported by the warm updrafts. In the entrainment zone, the negative heat flux is primarily associated with the cold updrafts. This flux is partially compensated by the positive heat flux resulting from correlated negative temperature and vertical velocity fluctuations in the cold downdrafts falling back down into the convectively mixed layer. From conditionally sampled u fluctuations (Fig. 22b), one can deduce that the horizontal velocity fluctuations with a negative sign near the CBL bottom are mainly attributed to updrafts, while downdrafts transport positive momentum fluctuations, which are smaller in magnitude. In combination, this provides a negative flux of the horizontal momentum in the lower portion of the CBL, (see Fig. 5b in Fedorovich *et al.* [15]). The sampling pattern with IF II gives evidence of the negative momentum transport across the inversion by large-scale motions. Nevertheless, the net vertical transport of momentum in the inversion layer is rather small.

Figure 23a testifies that in the lower portion of the simulated CBL the temperature excess of the warm updrafts is larger than that of the cool downdrafts. This feature of the CBL turbulence structure we have already pointed out while discussing the joint probability patterns in Fig. 20. Within the inversion layer, the net values of the temperature fluctuations are quite small due to the relatively weak inversion in the wind tunnel CBL, (see discussion to Fig. 15b). On the other hand, the temperature sampling with IF II provides noticeably larger magnitudes of negative temperature fluctuations in up- and downdrafts, which are both cooler than the surrounding air.

This allows to infer that the heat flux of entrainment in the wind tunnel CBL is maintained by comparatively small-scale and slow vertical motions, meanwhile the air from the larger-scale and faster updrafts is only slightly heated above the inversion before it sinks back into the mixed layer, (see also Fig. 22a).

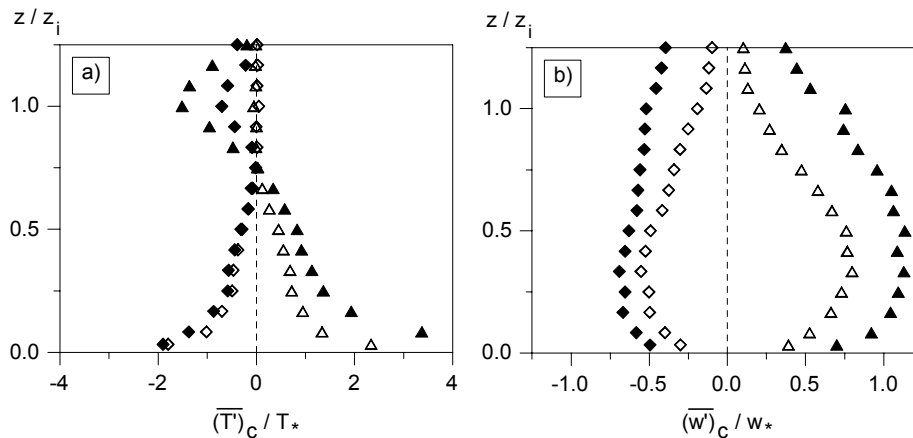


Figure 23. Conditionally sampled values of (a) temperature and (b) vertical velocity in the wind tunnel CBL at $x=3.98$ m. For notation see Fig. 22.

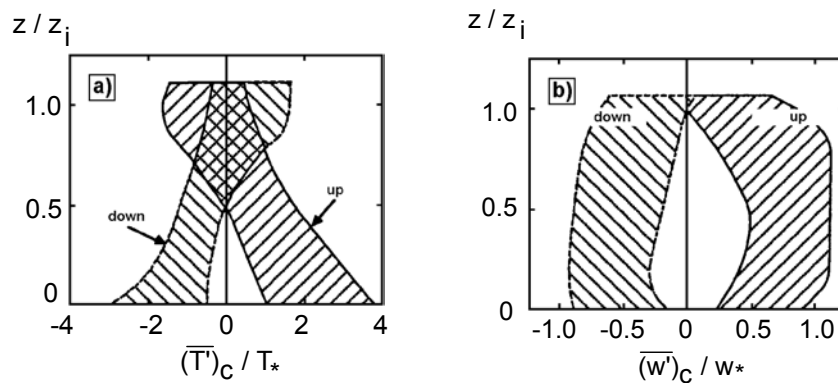


Figure 24. Conditionally sampled values of (a) temperature and (b) vertical velocity in the atmospheric CBL, after Greenhut and Khalsa [18], and Young [59].

Results of temperature sampling in the upper portion of the atmospheric CBL (Fig. 24a) show both positive and large temperature fluctuations in the atmospheric downdrafts. Apparently, this corresponds to CBL cases with strong capping inversions. The wide range of values indicated in Fig. 24a are related, in part, to different indicator functions used by different investigators (Stull [52]).

Conditionally sampled values of the vertical velocity from the wind tunnel (Fig. 23b) are well within the range of w sampled in the atmosphere (Fig. 24b). It is seen in both graphs that updrafts in the bulk of the CBL are characterized by higher absolute vertical velocity values than downdrafts. Near the CBL top, the magnitudes of w fluctuations in updrafts and downdrafts are equalized.

3.3. SPECTRAL ANALYSIS

3.3.1. Spectra Derivation from Measurement Data

We calculate spectral densities by the finite Fourier transforms of the original time series based on the Wiener-Khinchin relationship. This relationship equates the spectral densities to the one-sided spectral density functions defined in terms of Fourier transforms of correlation functions (Bendat and Piersol [3]). Since the introduction of algorithms for fast Fourier transforms by Cooley and Tukey [7], this approach towards the discrete spectra calculation has become dominant.

To average the spectra, an original time series consisting of 16384 data values was separated into 31 overlapping records, each containing 1024 measurement values. The calculated spectra were subdivided into 400 equal intervals with respect to the logarithm of frequency, and the average spectral density value within each interval was calculated. This was done merely to improve the layout of the spectra when plotted in logarithmic scales. For the details of spectra calculation see Kaiser and Fedorovich [23].

Since the Taylor hypothesis was found to be valid for the simulated CBL (Fedorovich *et al.* [15]), it was used to transfer the spectra from the frequency domain to the wavenumber one. Provided the mean-flow horizontal velocity u in the measurement location of spectrum is known, the following relationship between the wavenumber k , the wavelength λ , and the frequency f may be employed:

$$k = \frac{2\pi}{\lambda} = \frac{2\pi f}{u}. \quad (3)$$

The wavenumber spectrum $P_\varphi(k)$ and the frequency spectrum $P_\varphi(f)$ of a quantity φ are related by

$$P_\varphi(k) = \frac{u}{2\pi} P_\varphi(f). \quad (4)$$

Experimental spectra are usually presented with logarithmic scales of frequency or wavenumber (Jensen and Busch [21], Panofsky and Dutton [37]). If the ordinates are $fP_\varphi(f)$ or $kP_\varphi(k)$, then the area in a log-frequency or log-wavenumber interval represents the contribution of the fluctuations in this interval to the variance of φ . Another advantage of these ordinates is their independence on the selected units of frequency or wavenumber, because $fP_\varphi(f) = kP_\varphi(k)$. Most of the wind tunnel spectra are shown below in such a logarithmic frequency / wavenumber form.

3.3.2. Velocity and Temperature Spectra

We begin consideration of the turbulence spectra with the evaluation of the vertical to horizontal velocity spectral ratio P_w/P_u in the wind tunnel CBL. This characteristic is important for making assumptions concerning the local isotropy of turbulence and the existence of inertial subranges in the measured spectra. Both features should be taken into account when the TKE dissipation rate and the destruction rate of temperature fluctuations are evaluated from the measured spectra.

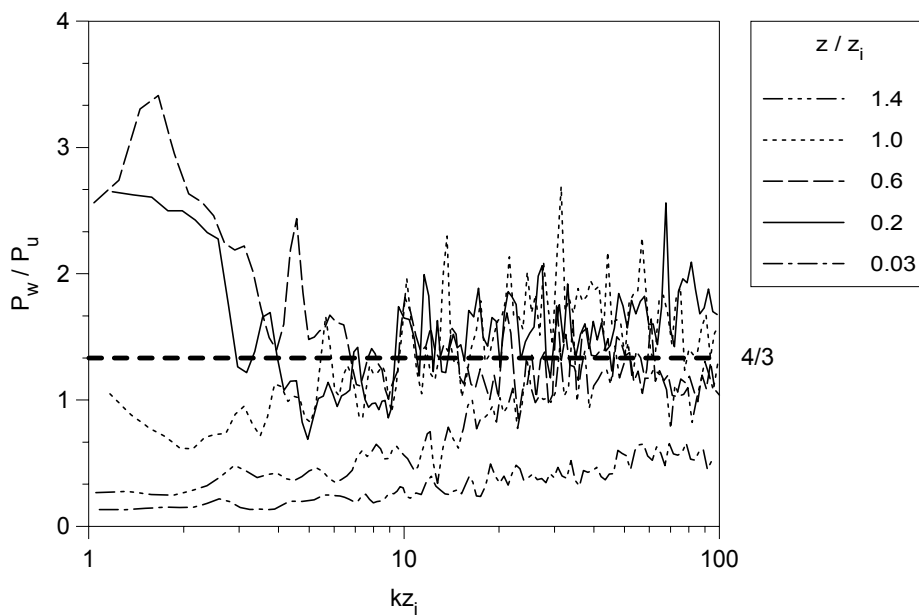


Figure 25. Spectral ratio P_w/P_u at different dimensionless elevations in the wind tunnel flow ($x=3.98$ m).

Kolmogorov [24] introduced the concept of inertial subrange as that of the energy cascade interval in the turbulence spectrum where no energy enters the system from the outside and no energy dissipates. Within this interval, the energy spectrum is isotropic, it does not depend on viscosity, and its shape is determined only by the energy flux over the spectrum which is equal to the energy dissipation rate ε . Thus, in the inertial subrange

$$P_i(k) \sim \varepsilon^{2/3} k^{-5/3},$$

where $P_i(k)$ is the spectral density of the velocity component u_i . Obukhov [35] has shown that the assumptions of the Kolmogorov [24] theory lead also to a $-5/3$ law for the inertial-subrange

spectrum of temperature fluctuations. Local isotropy of turbulence and the presence of the inertial subrange in spectra are conditioned by a sufficiently high turbulent Reynolds number of the flow, $Re_l = \mathbf{u}l/\nu$, where \mathbf{u} is the representative turbulence velocity scale, l is the integral turbulence length scale, and ν is the kinematic air viscosity. According to the analysis of Tennekes and Lumley [54], Re_l has to be of the order 10^3 and more to justify the employment of the Kolmogorov theory relationships for spectra in the inertial subrange.

In the wind tunnel, \mathbf{u} is of the order 0.1 m/s, and l is approximately 0.5 m (Fedorovich *et al.* [15]) which gives $Re_l \approx 3 \cdot 10^3$ (adopting $\nu = 1.5 \cdot 10^{-5} \text{ m}^2/\text{s}$). The characteristic wind tunnel value of the Reynolds number $Re_\lambda = \mathbf{u}\lambda/\nu$ based on the Taylor microscale λ is about 50. Here, the estimate $\lambda = 10^{-2} \text{ m}$ is obtained from $\lambda^2 = 15\nu\mathbf{u}^2/\varepsilon$, where ε is taken to be equal $10^{-2} \text{ m}^2/\text{s}^3$, (see section 3.3.3).

Under conditions of local isotropy, the Kolmogorov theory predicts the P_w/P_u ratio in the inertial subrange to be equal 4/3 (Mestayer [33]). The wind tunnel values of P_w/P_u are plotted against the dimensionless wavenumber kz_i in Fig. 25. With $kz_i > 10$, the P_w/P_u ratio in the main portion of the CBL is close to the local-isotropy value. It is possible to notice, however, that the average of P_w/P_u slightly exceeds the 4/3 criterion. Such a small, but persistent anisotropy of turbulent motions at comparatively large wavenumbers may be due to the insufficiency of the pressure fluctuations to isotropize turbulence in the presence of dominant buoyant forcing, which favors vertical motions (Schmidt and Schumann [48]). Nevertheless, it is seen from Fig. 25 that turbulence in the simulated CBL may be considered as approximately isotropic in the wavenumber range $10 < kz_i < 80$, and in the range of heights $0.2 \leq z/z_i \leq 1$.

Above the CBL, at $z/z_i = 1.4$, the local isotropy is observed only over a very short range of wavenumbers. Close to the surface, at $z/z_i = 0.03$, the turbulence is essentially anisotropic over the whole range of scales. In this portion of the flow, the horizontal motions dominate the vertical ones due to the damping effect of the surface. This is also a reason why the turbulence becomes more isotropic with decreasing scales of motion.

With dimensionless wavenumbers smaller than 10, the behavior of P_w/P_u differs in the CBL mixed core and in the inversion layer. In the mixed-layer, at $z/z_i = 0.2$ and $z/z_i = 0.6$, the P_w/P_u ratio reveals a strong turbulence anisotropy associated with the dominance of vertical motions. Within the inversion layer, at $z/z_i = 1$, the dependence of P_w/P_u on k supports our earlier findings concerning the vertical motion suppression at the CBL top, and the enhancement of the horizontal velocity fluctuations due to the sideward transport of air from the blocked thermals.

Comparison of the wind tunnel velocity spectra with the spectral data from the water tank study of Deardorff and Willis [9], and from the LES study by Schmidt and Schumann [48] is presented in Figs. 26a and 26b. In both studies considered here for comparison, the shear-free atmospheric CBL was modeled. The wind tunnel turbulence statistics have been compared with data from these studies in section 3.2.1. It has been shown there that u and w velocity component variances in the lower and middle portions of the wind tunnel CBL are relatively large. The spectral distribution of divergence between the wind tunnel, water tank, and LES velocity variances can be traced in the presented velocity component spectra.

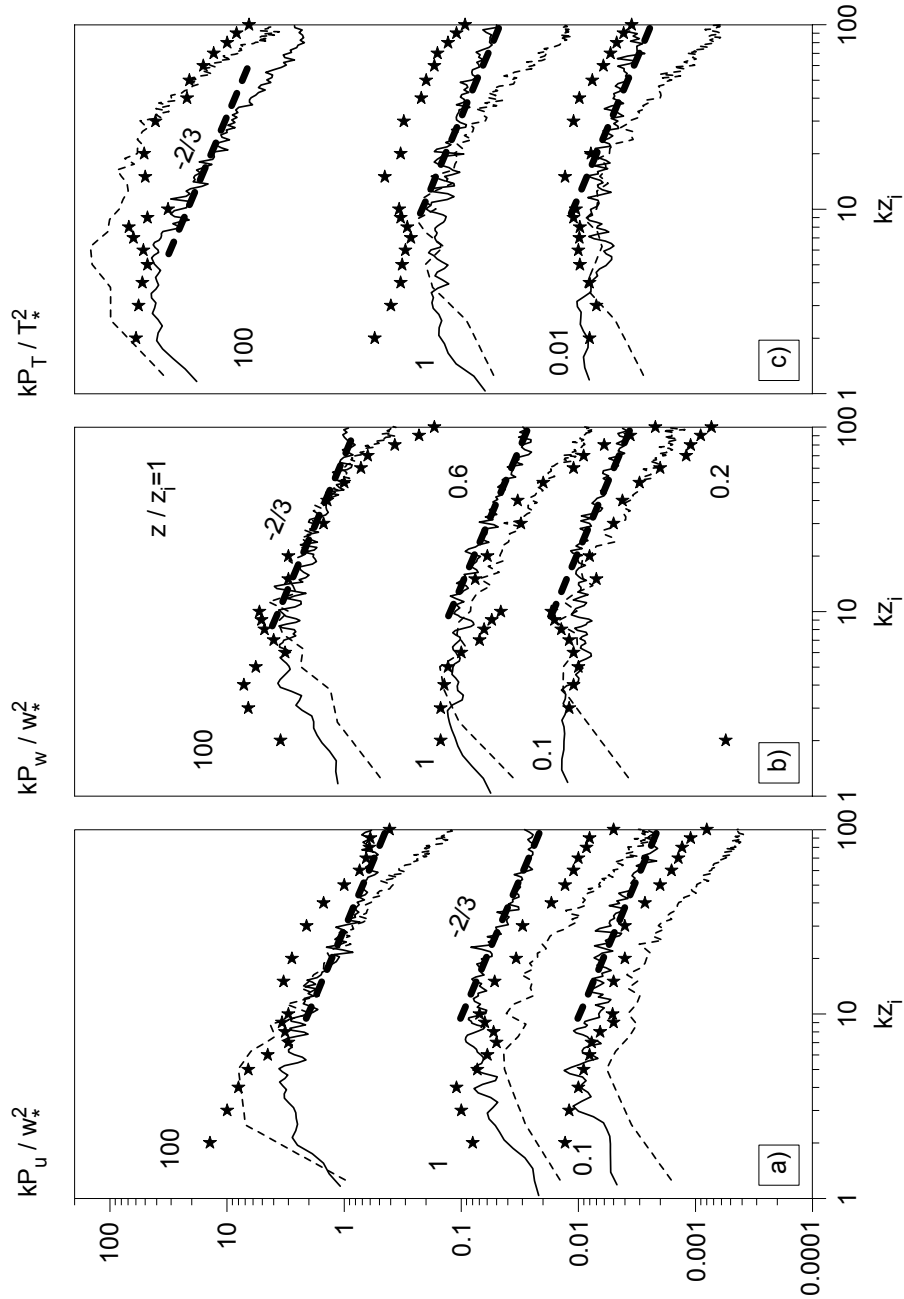


Figure 26. Spectra of (a) longitudinal velocity, (b) vertical velocity, and (c) temperature in the wind tunnel CBL, solid lines. Corresponding spectra from the water tank model of Deardorff and Willis [9], and from the LES study of Schmidt and Schumann [48] are given by stars and dashed lines, respectively.

At smaller wavenumbers ($kz_i < 8$), the wind tunnel u spectra (Fig. 26a) are positioned between the water tank and LES spectra. Comparatively large water tank spectra values in this wavenumber range presumably exhibit the effect of horizontal inhomogeneity of the surface heat flux first pointed out by Schmidt and Schumann [48], (see also discussion in section 3.2.1).

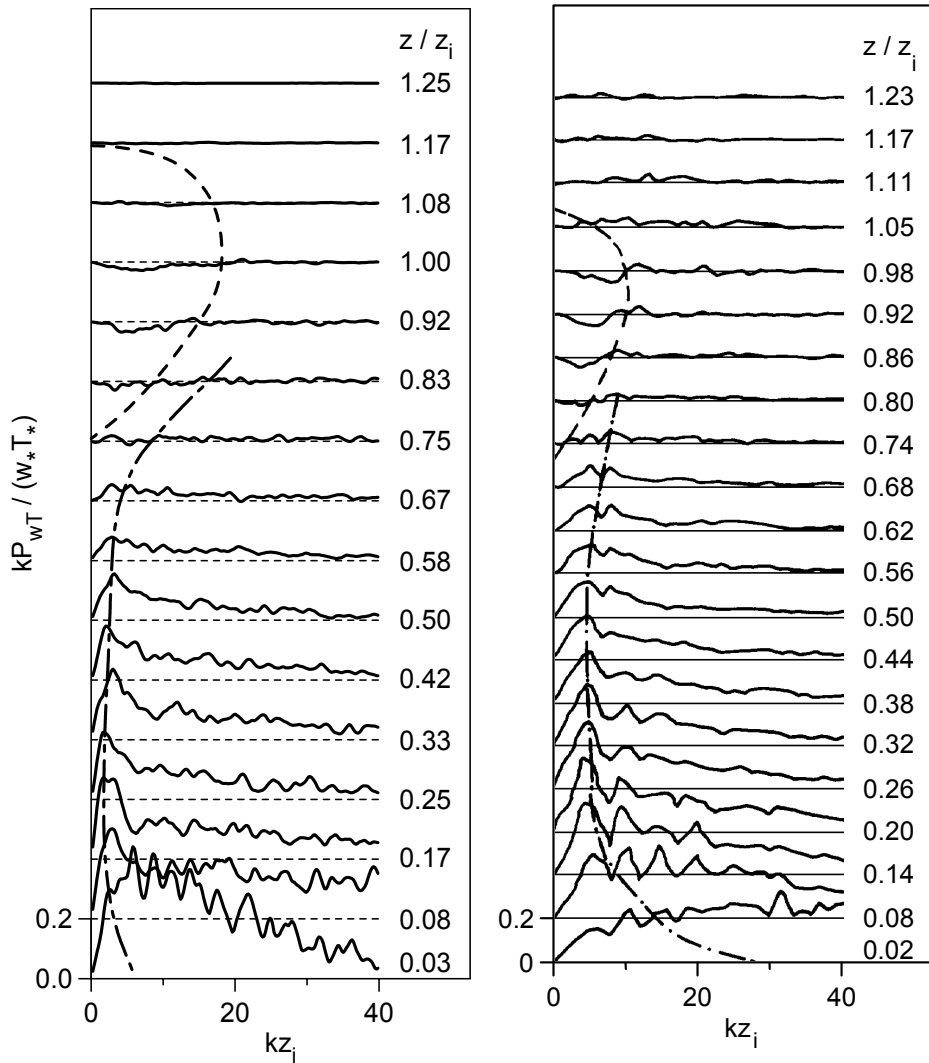


Figure 27. Spectra of the vertical turbulent heat flux from the wind tunnel model, left plot, and from the LES study of Schmidt and Schumann [48], right plot.

Larger w spectral values in the wind tunnel model at small wavenumbers may be explained by the shear contribution, and by the quasi-steady cellular circulations, which are both sources

of the velocity variance enhancement in the wind tunnel CBL (Fedorovich *et al.* [15]). Near the CBL top, at $z/z_i=1$, where the turbulence regime is practically unaffected by the surface shear, the wind tunnel spectra are close to the spectral curves from the other model studies.

At $z/z_i=0.2$ and $z/z_i=0.6$, the LES spectra decrease with an increasing wavenumber, while the wind tunnel spectral curves remain relatively flat. As a result, the wind tunnel spectra of both velocity components are larger than their water tank and LES counterparts with $kz_i > 10$. This suggests that in the lower portion of the CBL, the buoyancy acts as the dominant factor of turbulence production at smaller wavenumbers, while the contribution of shear becomes important with increasing wavenumbers. The joint effect of buoyant and shear forcings leads to the elongation of the production range and to the relative flatness of the normalized spectra in the high-wavenumber portion of this range. Such behavior of the velocity spectra in the sheared CBL is in accordance with the -1 power law predicted by Tschen [53] and Gisina [17].

At all altitudes represented in Fig. 26a, the normalized velocity spectra from the wind tunnel model display linear intervals at $kz_i > 10$, which can be approximated fairly well by the -5/3 (for the normalized spectra by -2/3) power laws of the Kolmogorov [24] inertial-subrange theory. These linear intervals, although clearly seen in the spectra, are rather short compared with the typical extensions of inertial subranges observed in the velocity spectra from atmospheric measurements (Kaiser and Fedorovich [23]).

The temperature spectra from the wind tunnel model are compared in Fig. 26c with T spectra from the water tank and LES studies. At the two lower elevations in the wind tunnel CBL, the temperature spectra shape is similar to those of u spectra shown in Fig. 26a. This bears evidence of a vast range of temperature fluctuation scales that almost equally contribute to the spectral energy. In the CBL core, the wind tunnel spectra are located close to the LES spectra, but are not as convex as the latter ones.

In the inversion layer, at $z/z_i=1$, the decay of the wind tunnel temperature spectrum in the high-wavenumber range is faster than in the spectra measured at lower levels. Here, the effect of inversion strength on the temperature fluctuation magnitude is clearly seen. The smaller inversion strength in the wind tunnel experiments is the reason for the lower position of the corresponding spectrum curve in Fig. 26c as compared with temperature spectra from the water tank and LES studies.

At larger wavenumbers, linear -5/3 intervals are observed in the wind tunnel temperature log-spectra. However, they are even shorter than the inertial subranges in the velocity spectra, (compare Fig. 26c with Figs. 26a and 26b).

Figure 27 presents the wind tunnel heat flux spectra (cospectra of the vertical velocity and temperature fluctuations) compared with the heat flux spectra from the LES study of Schmidt and Schumann [48]. At $z/z_i=0.03$, the influence of the surface shear in the wind tunnel CBL can be a reason for the comparatively weak correlation between w and T fluctuations at larger wavenumbers. We have already noted that under the influence of shear, the production ranges of w spectra are elongated towards higher frequencies. Velocity fluctuations produced by shear are not coupled with temperature fluctuations, rather they are merely stochastically mixed with them. This results in the comparatively fast decay of the heat flux spectrum with increasing wavenumbers.

In the middle portion of the CBL, the wind tunnel cospectra consistently exhibit comparatively broad spectral maxima related to the thermals (w' and T' are both positive), and

to cool downdrafts (w' and T' are both negative). These maxima are located within the wavenumber range from $kz_i=3$ to $kz_i=8$. The LES cospectra in the CBL core have their maxima approximately within the same range. This corresponds to the observation of Kaimal *et al.* [22], who found that motions with scales of the order of z_i are the main contributors to the turbulent transport of heat in the atmospheric CBL.

The magnitude of the cospectrum decreases towards the upper portion of the CBL, and the spectral maximum shifts to larger wavenumbers, (remember the decrease with height of the horizontal sizes of thermals in the visualized patterns of section 3.1.2). In the inversion layer, at $z/z_i > 0.8$, the heat flux spectra become negative with smaller wavenumbers. These negative spectral values mainly represent large-scale cool updrafts, which are the characteristic structures in the upper portion of the wind tunnel CBL. There are also warm downdrafts of the entrained air which are partially responsible for the negative cospectra values within the inversion layer. Higher-frequency components of the heat flux in the entrainment zone retain positive values and gradually decay towards the CBL top, (see the cospectrum at $z/z_i=1.2$).

3.3.3. Dissipation Rates of TKE and Temperature Fluctuations

For the evaluation of the TKE dissipation rate ε from the wind tunnel velocity spectra we employ the following relationships of the Kolmogorov inertial-subrange theory (Tennekes and Lumley [54]):

$$P_u(k) = \alpha \varepsilon^{2/3} k^{-5/3}, \quad (5)$$

$$P_w(k) = \frac{4}{3} \alpha \varepsilon^{2/3} k^{-5/3}, \quad (6)$$

where the value of the dimensionless parameter α is taken equal 0.52 (Andreas [2], and Schmidt and Schumann [48]). From a practical point of view, the procedure of the determination of ε is based on the least-square approximation of the inertial-subrange spectrum using Eqs. (5) and (6). The applicability of these equations to spectra obtained near the CBL top, where spectral inertial subranges are very short, seems to be rather questionable.

Vertical profiles of ε from the wind tunnel model are shown in Fig. 28a. We have seen in section 3.3.2 that the assumption of local isotropy is only approximately satisfied in the wind tunnel CBL. Thus we cannot expect horizontal and vertical velocity spectra to provide exactly the same values of ε . That is why, two wind tunnel ε values are given for each measurement level. In the main portion of the CBL, discrepancies between the dissipation rates, derived alternatively by Eq. (5) and by Eq. (6), are much smaller than the scatter of data from other sources represented in the plot. The smallest dissipation rate values originate from the Schmidt and Schumann [48] LES study of a pure shear-free CBL. Larger ε values in the lower portion of the water tank CBL of Deardorff and Willis [9] are presumably a result of the TKE overproduction due to the previously discussed horizontal variations of the bottom heat flux in their experiments. Dissipation rates measured in the ocean and in the atmosphere are apparently affected by nonbuoyant contributions to the TKE production. Comparatively large ε values in the wind tunnel CBL result from the combined influence of shear, cellular circulations, and

transition effects. All mentioned factors have already been considered earlier in the present paper.

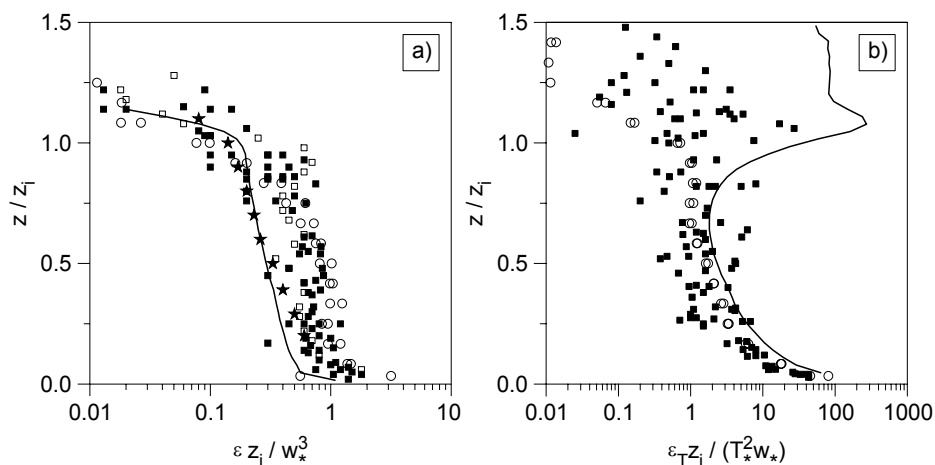


Figure 28. TKE dissipation rate (a), and destruction rate of temperature fluctuations (b) in the CBL. The wind tunnel data (circles) are compared with the atmospheric data from Caughey and Palmer [5], filled squares in (a), and Sorbjan [50], filled squares in (b); oceanic data of Shay and Gregg [49], empty squares; water tank model data of Deardorff and Willis [9], stars; and LES data (courtesy of U. Schumann), lines.

The temperature fluctuation destruction rate ε_T , (we define it here as destruction of the temperature half-variance), is obtained from the inertial-subrange temperature spectra using the Obukhov [35] law

$$P_T(k) = \beta \varepsilon_T \varepsilon^{-1/3} k^{-5/3}, \quad (7)$$

where $\beta=0.8$ is a dimensionless coefficient (Andreas [2], Schmidt and Schumann [48]). In Eq. (7), we have the choice of using ε determined either from Eq. (5) or from Eq. (6). It is clear, however, from Fig. 28b that the difference between the resulting ε_T profiles is small. This may be expected because $P_T(k)$ in Eq. (7) depends rather weakly on ε . In the lower half of the CBL, the discrepancies between ε_T from the three datasets represented in Fig. 28b are not very large. The drastic divergence of the ε_T profiles from different studies is observed in the upper portion of the CBL, where the turbulence regime is essentially governed by capping inversion effects. The wind tunnel model with weak inversion gives the smallest values of ε_T . The ε_T maxima in the atmospheric and LES profiles result from enhanced temperature fluctuations in the inversion layer with a strong stable temperature gradient (large $Ri_{\Delta T}$ numbers).

3.4. EFFECTS OF ELEVATED SHEAR

To study the effects of elevated shear on the CBL turbulence regime, the initial flow configuration shown in Fig. 29 was employed. The experimental setup parameters were as follows: the mean-flow temperature and velocity, of 20 K and 1 m/s, respectively, were kept height-constant within the two lower layers of the tunnel; at $z=0.3$ m, between the second and the third layers, a velocity increment of 0.5 m/s and a temperature increment of 30 K were imposed; throughout the upper layers the velocity was kept height-constant at 1.5 m/s, and the temperature increased vertically at a rate of 67 K/m. The heat flux through the bottom was the same as in the basic case studied (see section 3.1.1).

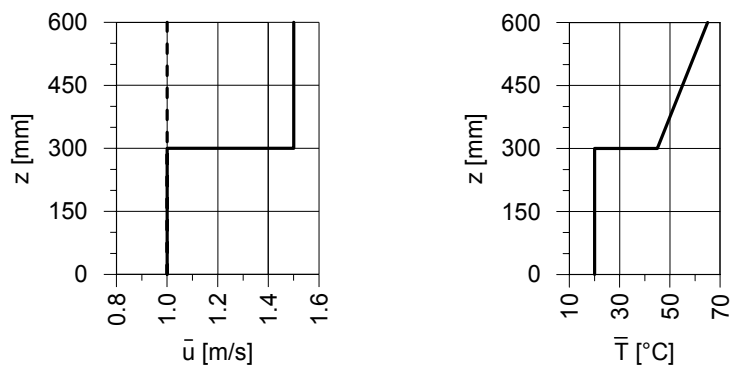


Figure 29. Velocity and temperature profiles at the test section inlet in the elevated-shear case study.

Results from the experiments with elevated shear are shown below in the non-normalized form. In the presence of elevated shear, the Deardorff [8] scaling, originally designed for the shear-free CBL driven by purely buoyant bottom-up forcing, is no longer relevant. We know of no scaling suggested for the CBL which appropriately accounts for effects of both the surface and elevated shears.

Modification of the TKE budget in the wind tunnel flow by elevated shear can be seen in Fig. 30. The main effect of the shear is an enhancement of the mechanical production of turbulence in the upper portion of the CBL. This production is balanced by the overall increase of the TKE dissipation rate. The thermal (buoyant) production of turbulence does not undergo considerable changes. It is possible to notice, however, that the buoyant production minimum, clearly seen near the CBL top in the case without elevated shear, decreases practically to zero in the presence of the shear and also shifts downwards. Our previous analysis has shown that the buoyant production minimum at the top of the wind tunnel CBL is primarily associated with cool updrafts penetrating aloft from the mixed layer, and to some extent also with the transport of heat down from the outer flow region by warm downdrafts (see section 3.2). Apparently, the elevated shear hampers the upward and downward motions at the CBL top and thus suppresses the heat exchange across the inversion layer. Under such conditions, the CBL growth associated with the penetration and entrainment processes, is considerably slowed down.

Such an impeded entrainment is clearly revealed by turbulence statistics measured at three subsequent stages of the CBL development, see Fig. 31. The capping inversion heights defined as the levels of most negative heat flux (Fig. 31a) progressively increase in the CBL without

elevated shear. Once shear is applied, the growth stops. A similar effect may be observed in the evolution of the position of the temperature variance maximum in Fig. 31b. In the inversion-capped CBL, this maximum approximately corresponds to the middle of the inversion layer (Fedorovich *et al.* [15]). Figure 31b also shows that the elevated shear reduces the magnitude of the temperature fluctuation in the inversion layer.

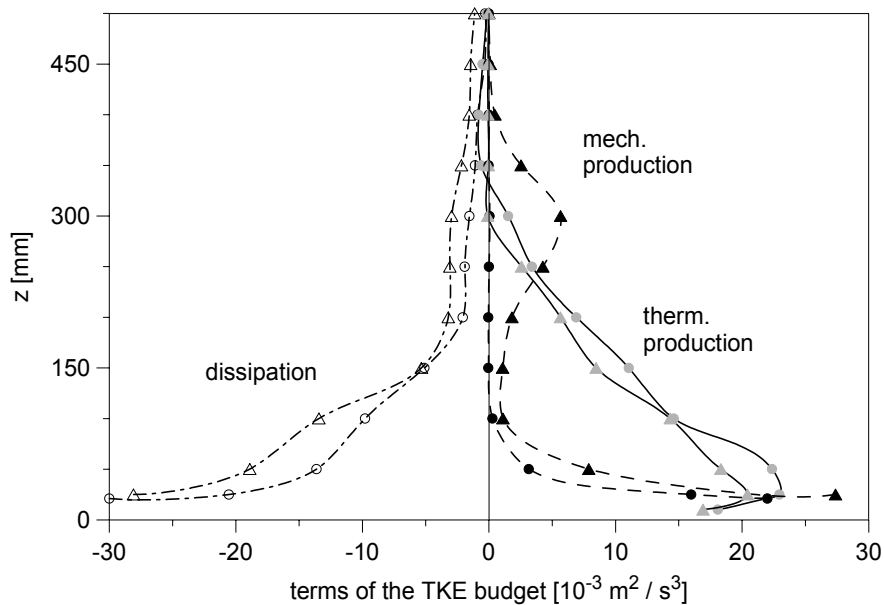


Figure 30. Main components of the TKE budget in the wind tunnel CBL with elevated shear (triangles) and without elevated shear (circles) at $x=7.28$ m.

Variances of the longitudinal and vertical velocities in Figs. 31c and 31d indicate that the turbulence production due to elevated shear is mainly attributed to the horizontal velocity fluctuations in the upper portion of the CBL, while the increase in the vertical velocity variance is relatively small.

Based on the data presented in Fig. 31, the following description of turbulence transformations in the sheared inversion layer may be outlined.

The imposed elevated shear deforms and partially dissolves the large-scale turbulence structures (up- and downdrafts) responsible for the vertical heat transport at the CBL top. This results in the enhancement of horizontal velocity fluctuations (see Fig. 31c) and leads to an energy redistribution between the larger-scale and smaller-scale vertical motions. The energy of the former decreases, and the energy of the latter increases. However, the integral of the vertical velocity spectrum (and thus also the vertical velocity variance) retains approximately the same value as in the shear-free inversion layer (Fig. 31d). Inside the entrainment layer, the smaller-scale vertical motions locally mix up the air from the destroyed convective structures. This can be an explanation for the smaller temperature variances at the CBL top as compared to the situation without elevated shear (Fig. 31b).

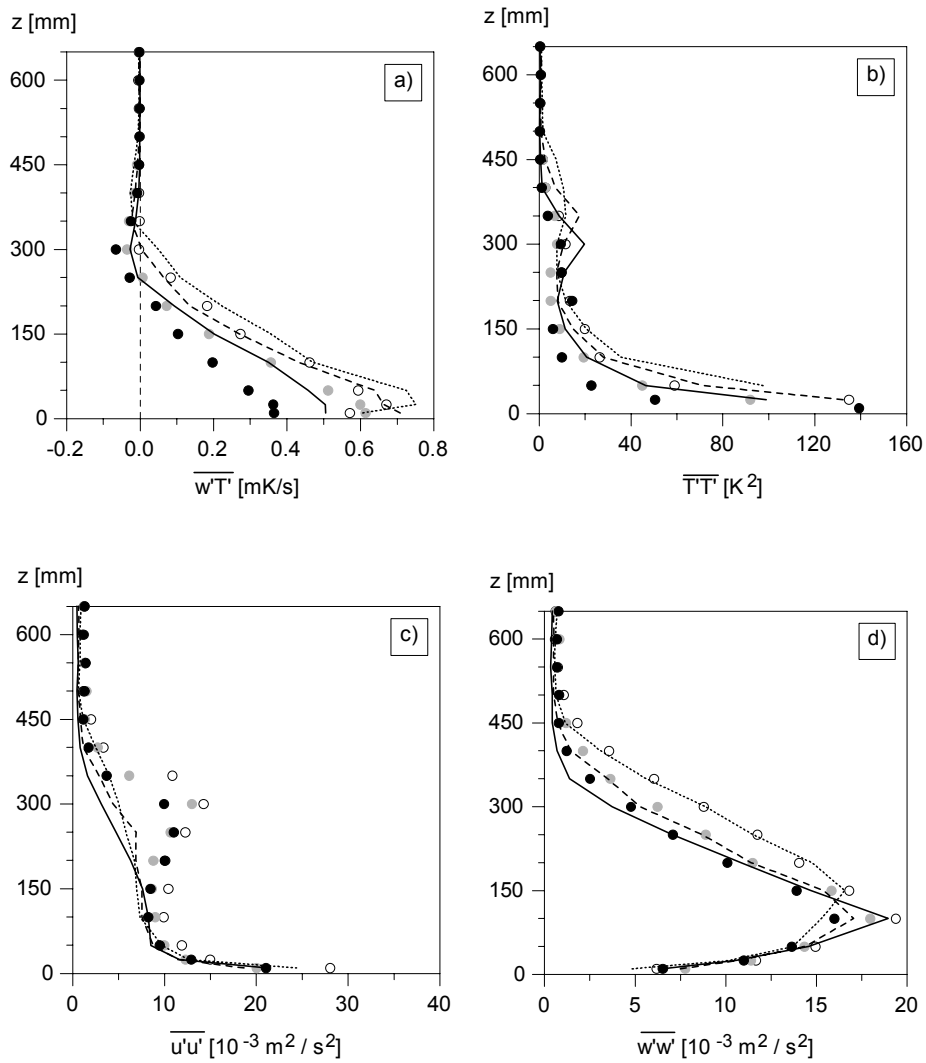


Figure 31. Vertical heat flux(d), and variances of (b) temperature, (c) longitudinal velocity, and (d) vertical velocity in the CBL with the elevated shear (points) and without the elevated shear (lines). Data refer to $x=3.98$ m (solid lines and black symbols), $x=5.63$ m (dashed lines and gray symbols), and to $x=7.28$ m (dotted lines and empty symbols).

A more profound insight into the turbulence mechanics within the sheared inversion layer could be provided by the spectral analysis of turbulence in this flow region. Such analysis is anticipated in the future program of wind tunnel experiments.

4. Summary and Conclusions

The presented results from the wind tunnel model study of the atmospheric CBL allow to conclude that the IHW thermally stratified wind tunnel adequately reproduces a number of important features of the atmospheric boundary-layer convective turbulence. Compared to water tank models of the CBL, the wind tunnel provides an advantageous opportunity to simulate the effects of combined buoyant and shear forcings in the atmospheric CBL.

The comparison of turbulence statistics and spectra, derived in the wind tunnel model by temporal averaging, with spatial averages from atmospheric, water tank and numerical CBL studies suggests that turbulence regimes in the nonsteady and horizontally evolving CBLs are similar to each other.

The Richardson numbers $Ri_{\Delta T}$ and Ri_N in the performed experiments corresponded to convective conditions in the atmosphere when both capping inversion and hydrostatic stability of the upper air are weak. Under such conditions, the negative heat flux of entrainment and the magnitude of the temperature fluctuations within the inversion layer are rather small. Also, the horizontal velocity variance decays almost monotonously throughout the inversion layer, with merely a slight bend in the profile.

We found that wind shears at the surface and across the inversion layer can essentially modify the regime of turbulence production in the CBL. The elevated shear turned out to be an inhibitor of entrainment at the CBL top. With the bottom-up buoyancy to shear production ratio u_* / w_* of 0.35 to 0.43, the turbulence variances in the lower portion of the CBL are noticeably larger than in the shear-free CBL.

Another mechanism of turbulence enhancement which mostly affects the wind tunnel CBL at the early stages of its development is associated with the transition from the nonmixed unstable convective layer in the neutral environment to the well-mixed CBL capped by a temperature inversion. The vertical velocity fluctuations in the middle part of the simulated CBL are additionally enhanced by the quasi-steady helical circulations.

Velocity spectra measured in the bulk of the CBL show that the buoyancy is the dominant factor of turbulence production at smaller wavenumbers, while the shear contribution increases with larger wavenumbers. The combined effect of buoyant and shear forcings in the simulated CBL could be a reason for the elongation and flatness of the production ranges of the spectra measured.

The vertical to horizontal velocity spectral ratio in the tunnel is slightly higher than the local-isotropy value of 4/3. The characteristic value of the turbulent Reynolds number Re_t in the wind tunnel CBL is $3 \cdot 10^3$. In the mixed core and in the entrainment zone of the simulated CBL, the log-spectra of velocity and temperature feature apparent linear -5/3 subranges at $kz_i > 10$. Nevertheless, the typical extension of the inertial subranges in the wind tunnel CBL is quite short. It is of the order of kz_i magnitude. The inertial-subrange theory relationships have been used for the evaluation of the turbulence dissipation rates from the velocity spectra.

The TKE dissipation rates in the simulated sheared CBL are comparatively large over the entire depth of the layer. The temperature fluctuation destruction rates from the wind tunnel model are close to the atmospheric values in the lower portion of the CBL. Within the inversion layer, the wind tunnel ε_T values are much smaller due to the weaker damping effect of the capping inversion.

In order to obtain information about the turbulence structure in the regions of the wind tunnel flow which are not accessible by the presently employed measurement technique, a parallel numerical study (LES) of the turbulence regime in the horizontally evolving atmospheric CBL is planned for the near future.

References

1. Adrian, R. J., Ferreira, R. T. D. S., and Boberg, T. (1986) Turbulent thermal convection in wide horizontal fluid layers, *Experiments in Fluids 4*, Springer-Verlag, 121-141.
2. Andreas, E. L. (1987) Spectral measurements in a disturbed boundary layer over snow, *J. Atmos. Sci.*, **44**, 1912-1939.
3. Bendat, J. S. and Piersol, A. G. (1986) *Random Data. Analysis and Measurement Procedures*, John Wiley & Sons.
4. Bruun, H. H. (1995) *Hot-Wire Anemometry*, Oxford University Press.
5. Caughey, S. J. and Palmer, S. G. (1979) Some aspects of turbulence structure through the depth of the convective boundary layer, *Quart. J. Roy. Meteor. Soc.*, **105**, 811-827.
6. Cenedese, A. and Querzoli, G. (1994) A laboratory model of turbulent convection in the atmospheric boundary layer, *Atmos. Environ.*, **28**, 1901-1914.
7. Cooley, J. W. and Tukey, J. W. (1965) An algorithm for the machine calculation of complex Fourier series, *Mathematics of Computation*, **19**, 297-301.
8. Deardorff, J. W. (1970) Convective velocity and temperature scales for the unstable planetary boundary layer and for Raleigh convection, *J. Atmos. Sci.*, **27**, 1211-1213.
9. Deardorff, J. W. and Willis, G. E. (1985) Further results from a laboratory model of the convective planetary boundary layer, *Bound.-Layer Meteor.*, **32**, 205-236.
10. Deardorff, J. W., Willis, G. E., and Lilly, D. K. (1969) Laboratory investigation of non-steady penetrative convection, *J. Fluid Mech.*, **35**, 7-31.
11. Deardorff, J. W., Willis, G. E., and Stockton, B. H. (1980) Laboratory studies of the entrainment zone of a convectively mixed layer, *J. Fluid Mech.*, **100**, 41-64.
12. Domnik, J. (1991) Application of LDA in gas flows, *Advanced Laser-Doppler Anemometry*. UMIST, University of Manchester, 1-25.
13. Drain, L. E. (1980) *The Laser Doppler Technique*, John Wiley & Sons.
14. Durst, F., Melling, A., and Whitelaw, J. H. (1987) *Theorie und Praxis der Laser-Doppler-Anemometrie*, Verlag G. Braun.
15. Fedorovich, E., Kaiser, R., Rau, M., and Plate, E. (1996) Wind tunnel study of turbulent flow structure in the convective boundary layer capped by a temperature inversion, *J. Atmos. Sci.*, **53**, 1273-1289.
16. Fedorovich, E. E. and Mironov, D. V. (1995) A model for shear-free convective boundary layer with parameterized capping inversion structure, *J. Atmos. Sci.*, **52**, 83-95.
17. Gisina, F. A. (1966) The effect of mean velocity and temperature gradients on the spectral characteristics of turbulence, *Izv. Acad. Sci. U. S. S. R., Atmos. Oceanic Phys.*, **2**, 804-813 (Engl. Transl., 487-491.)
18. Greenhut, G. K. and Khalsa, S. J. S. (1987) Convective elements in the marine atmospheric boundary layer. Part I: Conditional sampling statistics, *J. Clim. Appl. Meteor.*, **26**, 813-822.
19. Holtslag, A. A. M. and Nieuwstadt, F. T. M. (1986) Scaling the atmospheric boundary layer, *Bound.-Layer Meteor.*, **36**, 201-209.

20. Hooper, W. P. and Eloranta, E. W. (1986) Lidar measurements of wind in the planetary boundary layer: the method, accuracy and results from joint measurements with radiosonde and kytoon, *J. Climate Appl. Meteor.*, **25**, 990-1001.
21. Jensen, N. O. and Busch, N. E. (1982) Atmospheric turbulence, in E. J. Plate (ed.), *Engineering Meteorology*, Elsevier, pp. 179-231.
22. Kaimal, J. C., Wyngaard, J. C., Haugen, D. A., Coté, O. R., Izumi, Y., Caughey, S. J., and Readings, C. J. (1976) Turbulence structure in a convective boundary layer, *J. Atmos. Sci.*, **33**, 2152-2169.
23. Kaiser, R. and Fedorovich, E. (1998) Turbulence spectra and dissipation rates in a wind tunnel model of the atmospheric convective boundary layer, *J. Atmos. Sci.*, **55**, 580-594.
24. Kolmogorov, A. N. (1941) Local structure of turbulence in the incompressible fluid at very high Reynolds numbers, *Dokl. Akad. Nauk S.S.S.R.*, **30**, 299-303.
25. Kumar, R. and Adrian, R. J. (1986) Higher order moments in the entrainment zone of turbulent penetrative thermal convection, *J. Heat Trans.*, **108**, 323-329.
26. Lenschow, D. (1998) Observations of clear and cloud-capped convective boundary layers and techniques for probing them. See this volume.
27. Lenschow, D. H. and Stephens, P. L. (1980) The role of thermals in the convective boundary layer, *Bound.-Layer Meteor.*, **19**, 509-532.
28. Lenschow, D. H., Wyngaard, J. C., and Pennel, W. T. (1980) Mean-field and second-momentum budgets in a baroclinic, convective boundary layer, *J. Atmos. Sci.*, **37**, 1313-1326.
29. Lomas, C. G. (1986) *Fundamentals of Hot Wire Anemometry*, Cambridge University Press.
30. Mahrt, L. and Paumier, J. (1984) Heat transport in the atmospheric boundary layer, *J. Atmos. Sci.*, **41**, 3061-3075.
31. Meroney, R. N. (1998) Wind tunnel simulation of convective boundary layer phenomena. Simulation criteria and operating ranges of laboratory facilities. See this volume.
32. Meroney, R. N. and Melbourne, W. H. (1992) Operating ranges of meteorological wind tunnels for the simulation of convective boundary layer (CBL) phenomena, *Bound.-Layer Meteor.*, **61**, 145-174.
33. Mestayer, P. (1982) Local isotropy and anisotropy in a high-Reynolds-number turbulent boundary layer, *J. Fluid. Mech.*, **125**, 475-503.
34. Nelson, E., Stull, R., and Eloranta, E. (1989) A prognostic relationship for entrainment zone thickness, *J. Appl. Meteorol.*, **28**, 885-903.
35. Obukhov, A. M. (1949) Structure of the temperature field in turbulent flows, *Izvestiya Akad. Nauk S.S.S.R., Ser. Geogr. i Geofiz.*, **13**, 58-69.
36. Ogawa, Y., Diosey, P. G., Uehara, K., and Ueda, H. (1981) A wind tunnel for studying the effects of thermal stratification in the atmosphere, *Atmos. Environ.*, **15**, 807-821.
37. Panofsky, H. A., and Dutton, J. A. (1984) *Atmospheric turbulence*, John Wiley & Sons.
38. Paranthoen, P., Petit, C., and Lecordier, J. C. (1982) The effect of the thermal prong-wire interaction on the response of a cold wire in gaseous flows (air, argon and helium), *J. Fluid. Mech.*, **124**, 457-473.
39. Perry, A. E. (1982) *Hot-Wire Anemometry*, Clarendon Press, Oxford.
40. Plate, E. J. (1998) Convective boundary layer: a historical introduction. See this volume.
41. Poreh, M. and Cermak, J. (1984) Wind tunnel simulation of diffusion in a convective boundary layer, *Bound.-Layer Meteor.*, **30**, 431-455.

42. Poreh, M., Rau, M., and Plate, E. (1991) Design considerations for wind tunnel simulations of diffusion within the convective boundary layer, *Atmos. Environ.*, **25A**, 1250-1257.
43. Rau, M., Bächlin, W., and Plate, E. (1991) Detailed design features of a new wind tunnel for studying the effects of thermal stratification, *Atmos. Environ.*, **25A**, 1258-1263.
44. Rau, M. and Plate, E. (1995) Wind tunnel modelling of convective boundary layers, in J. E. Cermak, A. G. Davenport, E. J. Plate and D. X. Viegas (eds.), *Wind Climate in Cities*, Kluwer, pp. 431-456.
45. Rey, C., Schon, J. P., and Mathieu, J. (1979) Buoyancy effects in a wind tunnel simulation of the atmospheric boundary layer, *Phys. Fluids*, **22**, 1020-1028.
46. Ruck, B. (1987) *Laser-Doppler-Anemometrie*, AT-Fachverlag.
47. Sandborn, V. A. (1972) *Resistance Temperature Transducers*. Metrology Press, Fort Collins, Colorado.
48. Schmidt, H. and Schumann, U. (1989) Coherent structure of the convective boundary layer derived from large-eddy simulations. *J. Fluid. Mech.*, **200**, 511-562.
49. Shay, T. J. and Gregg, M. C. (1986) Convectively driven turbulent mixing in the upper ocean, *J. Phys. Oceanogr.*, **16**, 1777-1798.
50. Sorbjan, Z. (1991) Evaluation of local similarity functions in the convective boundary layer, *J. Appl. Meteor.*, **30**, 1565-1583.
51. Strickert, H. (1974) *Hitzdraht- und Hitzfilmanemometrie*, VEB Verlag Technik, Berlin.
52. Stull, R. B. (1988) *An Introduction to Boundary Layer Meteorology*, Kluwer Academic Publishers, Dordrecht.
53. Tschen, C. M. (1953) On the spectrum of energy in turbulent shear flow, *J. Res. NBS*, **50**, 51-62.
54. Tennekes, H., and Lumley, J. L. (1982) *A First Course in Turbulence*, The MIT Press.
55. Wiedemann, J. (1984) *Laser-Doppler-Anemometrie*, Springer-Verlag, Berlin.
56. Willis, G. E. and Deardorff, J. W. (1974) A laboratory model of the unstable planetary boundary layer, *J. Atmos. Sci.*, **31**, 1297-1307.
57. Willis, G. E. and Deardorff, J. W. (1976) On the use of Taylor's translation hypothesis for diffusion in the mixed layer, *Quart. J. Roy. Meteor. Soc.*, **102**, 817-822.
58. Wyngaard, J. C. (1992) Atmospheric turbulence, *Ann. Rev. Fluid Mech.*, **24**, 205-233.
59. Young, G. S. (1988) Turbulence structure of the convective boundary layer, *J. Atmos. Sci.*, **45**, 727-735.
60. Zilitinkevich, S. S. (1991) *Turbulent Penetrative Convection*, Avebury Technical, Aldershot.